

This is a repository copy of *Predictive process diagram for parameters selection in laser powder bed fusion to achieve high-density and low-cracking built parts*.

White Rose Research Online URL for this paper: https://eprints.whiterose.ac.uk/id/eprint/233286/

Version: Published Version

Article:

Phan, M.A.L. orcid.org/0000-0001-7744-1742, Dew, O. orcid.org/0009-0006-3026-0008 and Todd, I. orcid.org/0000-0003-0217-1658 (2024) Predictive process diagram for parameters selection in laser powder bed fusion to achieve high-density and low-cracking built parts. Additive Manufacturing, 85. 104145. ISSN: 2214-8604

https://doi.org/10.1016/j.addma.2024.104145

Reuse

This article is distributed under the terms of the Creative Commons Attribution (CC BY) licence. This licence allows you to distribute, remix, tweak, and build upon the work, even commercially, as long as you credit the authors for the original work. More information and the full terms of the licence here: https://creativecommons.org/licenses/

Takedown

If you consider content in White Rose Research Online to be in breach of UK law, please notify us by emailing eprints@whiterose.ac.uk including the URL of the record and the reason for the withdrawal request.



ELSEVIER

Contents lists available at ScienceDirect

Additive Manufacturing

journal homepage: www.elsevier.com/locate/addma





Predictive process diagram for parameters selection in laser powder bed fusion to achieve high-density and low-cracking built parts

Minh Anh Luan Phan*, Oliver Dew, Iain Todd

Department of Materials Science and Engineering, The University of Sheffield, Sir Robert Hadfield Building, Sheffield S1 3JD, United Kingdom

ARTICLE INFO

Keywords:
Normalised process diagrams
Right-first-time
Parameter prediction
Laser powder bed fusion
Hot cracking

ABSTRACT

The laser powder bed fusion process (LPBF) has been widely used in many industrial sectors, including automotive, aerospace, and biomedical devices. With the fast development of new materials designed for critical applications, the conventional design of experiments for determining an optimal LPBF process window is a time and material-consuming activity. This can impose difficulties on small-to-medium industrial businesses where investing resources are limited. To address these challenges, this study draws inspiration from a reliable diagram used in laser welding to construct a similar diagram for the LPBF process. The objective is to enable the "rightfirst-time" selection of parameters that achieve a minimum of 99% density, regardless of the metallic materials and machine platforms. The diagram is established based on dimensionless beam power and velocity, derived from multiple LPBF process parameters (e.g., laser power, scan speed, hatch spacing) and the thermophysical properties of materials (e.g., melting point, density, thermal diffusivity). Furthermore, hot cracking susceptibility is considered by a strain-rate approach incorporated with the dimensionless thermal strain factor, which benefits when processing hard-to-weld alloys. The diagram shows high reliability in determining parameters corresponding to lack of fusion, keyhole porosity and 99% dense parts when plotting against literature data of LPBF for several metallic materials. Similar results were observed when applying to a novel material ABD-900AM Nibased alloy, for which no previously published data were available. Moreover, the diagram proved effective in selecting parameters to process the high-cracking susceptible CM247LC Ni-based alloy, resulting in significant mitigation of hot cracking in the as-fabricated parts.

1. Introduction

1.1. Current methods to identify the laser powder bed fusion process parameters

In the Laser Powder Bed Fusion (LPBF) process, parameters are often selected through iterations of experiments using Design of Experiment (DOE) techniques such as Response Surface Methodology (RSM) [1–3] or the Taguchi method [2]. Multiple parameters, referred to as factors (e.g., laser power, scanning speed, hatch spacing, or layer thickness), are statistically evaluated against the desired output properties, known as responses (e.g., part density, surface roughness, or build rate). For new materials, the DOE procedure begins with a screening design encompassing the widest range of equipment capabilities, followed by further refinements using RSM. The resulting parameter combination is then validated to obtain the optimal settings [1]. When running experimental designs, cuboidal or cylindrical samples are often chosen for the ease of

following metallurgical preparation steps. However, further parameter modifications may be required to apply the optimal settings on different part geometries such as tensile samples or complex geometry components.

Data-driven process parameter selection has been increasing in attention recently. Druzgalski et al. [4] proposed a computational approach that divides scanning trajectories into smaller sections based on local laser-powder interactions. Each section is then mapped to its respective optimal parameters stored in libraries of models which will then be exported depending on the processing geometry. Populating these libraries requires other advanced thermal-mechanical and multi-physics simulations, thereby increasing resource usage and computational costs. Yeung et al. [5] implemented a Geometric Conductance Factor (GCF) to control the laser power concerning the local variation of thermal conductivity based on the solid-powder ratio. The approach demonstrated a better surface roughness on samples with the controlled model applied, however, the improvement was not

E-mail address: m.phan@sheffield.ac.uk (M.A.L. Phan).

^{*} Corresponding author.

greatly significant.

Numerical models have emerged as valuable tools in laser processing, providing reliable predictions for the kinetics of structural changes [6], microstructure evolution, and hardness variations within heat-affected zones [7] across different steel types. These models typically involve calculating the induced thermal field using analytical equations, which are then utilised in subsequent computations for microstructural predictions. Later, Ion et al. [8] further developed and converted these models into a series of dimensionless numbers. This novel approach enables the effective characterisation of laser processing parameters and facilitates the analysis of a wide range of materials, accounting for their specific thermo-physical properties. The resulting processing diagram proves to be exceptionally useful in determining optimal regions associated with desired outcomes, such as hardening, melting, or achieving specific keyholing depths.

The calculation of normalised enthalpy and normalised depth has proven to be an effective approach in predicting various welding modes for laser-welded materials [9]. This methodology was also adapted by King et al. [10] for the LPBF process of 316 L stainless steel to estimate keyhole thresholds. Rubenchik et al. [11] developed simple scaling laws based on normalised enthalpy and melt depth for different materials and LPBF platforms. Yang et al. [12] proposed a scaling law to establish a correlation between the melt pool width and process parameters. However, these studies have overlooked several important parameters of the LPBF process, including hatch spacing, layer thickness, and scan strategies. By considering only single scanning lines, which aligns with welding practices, these investigations fail to fully capture the complex processing conditions inherent to the LPBF process.

Grouping major variables of metallic additive manufacturing (AM) processes and material properties into dimensionless numbers offers a comprehensive approach to comprehending the AM process [13]. Mukherjee et al. [14] investigated the use of dimensionless numbers such as Fourier, Peclet, and Marangoni numbers on the achievement of high part density, mitigating thermal distortion, and controlling solidified microstructure. However, calculating these dimensionless numbers necessitates the development of well-tested 3D transient heat transfer and fluid flow models, which can be computationally demanding for the LPBF process [4]. To address this, Thomas et al. [15] introduced normalised model-based processing diagrams for AM techniques, an extension of laser processing diagrams originally introduced by Ion et al. [8]. These diagrams incorporate additional dimensionless factors, such as layer thickness and hatch spacing, which are crucial LPBF parameters. The normalised processing diagrams demonstrate good agreement with existing literature data on process windows for well-studied metallic alloys in AM powder bed fusion. However, their applicability is limited when dealing with new materials as they lack predictive capabilities.

Establishing an optimal process window for a specific metallic alloy is a time-consuming and resource-intensive task, regardless of the methodology employed. The literature review reveals that using dimensionless numbers, which combine process parameters and materials properties, offers a comprehensive approach. However, establishing a clear relationship between desired outcomes (such as part density and low cracking density) and the input dimensionless numbers is crucial. Notably, the work of Ion et al. [8] has demonstrated effectiveness in predicting input parameters and desired results for laser welding, including hardening, melting, and keyholing depths. Furthermore, Thomas et al. [15] have validated the applicability of the model to additive layer manufacturing.

In this study, we utilised the model developed by Ion et al. [8] briefly overviewed in Section 1.2, followed by a consideration and incorporation of specific processing characteristics of the LPBF process into the model to enhance its compatibility (Section 1.3). Additionally, we integrated an additional dimensionless factor, the thermal strain factor, proposed by Mukherjee et al. [16], to assess thresholds for hot cracking density (Section 1.4). To validate the model, we compared its predictions with existing literature data and experimental results conducted

in-house. Finally, the model was applied to a nickel-based legacy alloy, CM247LC (known for its high hot cracking susceptibility), to evaluate its capability in selecting process parameters for achieving 99% density and minimizing hot cracking density in the produced parts. The nomenclature list that defines all the symbols used throughout the study is shown in Table 1

1.2. The original normalised laser process diagram

In this section, the definition of dimensionless numbers and the construction of the laser process diagram from the work of Ion et al. [8] are overviewed. For a given material and laser parameters, Ion et al. [8] defined two dimensionless numbers that group important parameters of laser processing:

Dimensionless beam power q^* :

$$q^* = \frac{A.q}{r_B.\lambda.(T_m - T_0)} \tag{1}$$

Dimensionless beam velocity v^* :

$$v^* = \frac{v \cdot r_B}{\alpha} \tag{2}$$

Room temperature values are mainly selected for λ and α for the ease of data acquisition. For the build set up using a preheated baseplate, λ and α were selected at that specific preheat temperatures. In LPBF, the effective surface absorptivity A is a sensitive factor that can affect the calculation of the dimensionless numbers. Ye et al. [17] found that A is strongly affected by laser power, scan speed and beam diameter in the keyhole regime and slightly by the powder thickness. The absorptivity can increase up to 0.7 when the laser power increases as the keyholing mode transition occurs causing rigorous interaction between the laser beam and the molten metal surface within the keyhole cavity [17,18]. In contrast, increasing the scan speed was found to greatly reduce the surface absorptivity.

For the conduction mode, the surface absorptivity shows a strong dependence on the powder thickness. In this study, the conduction

 Table 1

 Nomenclature list of symbols and units used in the study.

Input laser power (W)

ζ/ν. Characteristic time (s)

Surface absorptivity

A	Surface absorptivity
r_B	Beam radius (mm)
ν	Scanning speed (mm/s)
1	Layer thickness (mm)
h	Hatch spacing (mm)
L	Scan length (mm)
с	Specific heat capacity (J/gK)
ρ	Density (g/mm ³)
λ	Thermal conductivity (W/mmK)
α	Thermal diffusivity (mm ² /s)
T_m	Melting temperature (K)
T_{ν}	Vaporising temperature (K)
T_{O}	Powder bed or next track's temperature (K)
$T_{preheat}$	Preheat temperature (K)
z	Induced depth below surface by the Gaussian laser beam (mm)
z_0	Characteristic distance to limit the surface temperature to a finite value due
	to the finite heat injection time (mm)
t	Time (s)
t_0	$r_B^2/4\alpha$, characteristic heat transfer time (s)
t_r	Returning time (s)
L_m	Latent heat of fusion (J/g)
ε_{max}	Maximum thermal strain (%)
ε_{crit}	Critical thermal strain (%)
dε∕dT	Critical thermal strain over temperature drop
β	Coefficient of volumetric thermal expansion
ΔT	Difference between melting point T_m and surrounding temperature T_0
H	P/ν , heat input per unit length (J/mm)
EI	Flexural rigidity (E is elastic modulus and I is the second moment of inertia)
F	$\alpha \tau / \zeta^2$, Fourier number
ζ	Characteristic melt pool length (mm)

q, P

Table 2Absorptivity values of different powder layer thicknesses used for the calculation.

Powder layer	Absorptivity				
30 μm to 50 μm	0.3				
50 μm to 70 μm	0.35				
70 μm to 100 μm	0.45				

regime will be used to match the temperature field analysis proposed in the work of Ion et al. [8], thus the respective surface absorptivity is approximated accordingly. The value of *A* for nickel-based, titanium-based, and stainless steel will be selected based on the use of powder layer thickness [17], as shown in Table 2.

For materials such as pure copper and molybdenum, the effect of powder thickness on laser absorptivity has been rarely reported in the literature, thus specific values were selected for copper as 0.3 [19] and molybdenum as 0.656 [20].

A laser process diagram was then constructed based on the normalised temperature field, T^* , to determine the processing boundaries (onset melting or vaporising). These boundaries were used for plotting the calculated dimensionless q^* and ν^* to evaluate if the parameter sets meet the required processing conditions (e.g., melting or vaporising). The mathematical relationship between T^* , q^* , and ν^* at an induced depth z^* is shown below:

$$T^* = \frac{(T - T_0)}{(T_m - T_0)} = \frac{\left(\frac{2}{\pi}\right) \times \left(\frac{q^*}{\nu^*}\right)}{\left[t^*(t^* + 1)\right]^{\frac{1}{2}}} \times \exp\left[\frac{\left(z^* + z_0^*\right)^2}{t^*}\right]$$
(3)

where $z^* = z/r_B$ is the dimensionless depth, $z_0^* = z_0/r_B$ is the dimensionless offset distance [8] and $t^* = t/t_0$ is the dimensionless time. The calculation of t^* and z_0^* is referred to the original work of Ion et al. [8] and Shercliff and Ashby [21]. Details of the construction of the LPBF diagram are shown in Appendix A.

1.3. Adapting the normalised model to the LPBF process

In Eq. (3), a $T^*_m=1$ represents the surface peak temperature at the melting point T_m , and a $T^*_\nu=2$ is approximated based on the onset vaporisation temperature Tv, which tends to be approximately twice that of Tm for many metals and alloys [22]. Considering a schematic illustration of the LPBF process in Fig. 1, consolidation of powder material is obtained when the laser beam successfully melted at least one powder layer l to create bonding with the previous layer.

To melt one powder layer l, the value for q^* can be calculated from Eq. (3) based on $z^* = l/r_B$ and $T^*_m = 1$. The heat energy required for melting is the sum of the net power to raise the material to the melting temperatures and the latent heat of fusion. In dimensionless terms, the net power q^*_{net} can be calculated for a given v^* as follows:

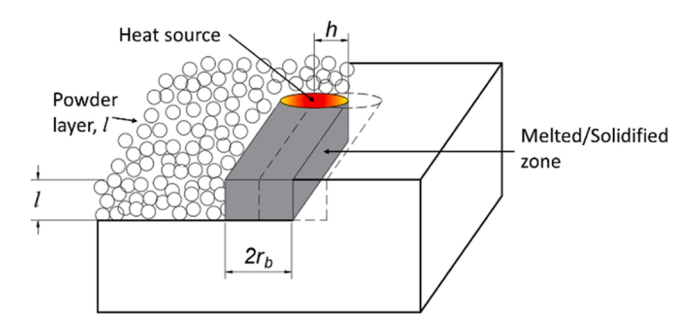


Fig. 1. Schematic illustration of the powder consolidation in the LPBF process, adapted from Fig. 3 in [15].

$$q_{net}^* = \left(-2z^*L_m^* + \frac{T_{m/\nu}^* \times [t^*(t^*+1)]^{\frac{1}{2}}}{(\frac{2}{\pi})} \times \exp\left[\frac{(z^*+z_0^*)^2}{t^*}\right]\right) \times \nu^*$$
 (4)

where $L^*_m = L_m / [c(T_{m/\nu} - T_0)]$ is the normalised volumetric latent heat of fusion. The value of L^*_m lies around 0.39 according to reference [22]. Similarly, the q^*_{net} required to raise material to its vaporising temperature can be figured out simply by replacing $T^*_{\nu} = 2$ in Eq. (4). By applying Eq. (4) to a range of ν^* corresponding to the LPBF platform's scan speed capability, the melting or vaporising boundaries can be defined. As a result, parameter sets (q^*, ν^*) located below the melting boundary will cause lack of fusion; above the vaporisation, the boundary will tend to create keyhole porosity; and between the boundaries are good processing parameters.

1.4. Consideration of scan length and hatch spacing

The original normalised laser process diagram proposed by Ion et al. [8] has been slightly modified to align with the LPBF processing conditions. However, typical variables, such as scan length L and hatch spacing h, have not been addressed yet. The former reflects the geometrical effect and together with the latter accounts for the unique characteristic of heat accumulation during track-by-track scanning. Changes in L and h will impact the temperature distribution in the vicinity of the laser beam. In this investigation, a temperature denoted as T_0 is calculated using the Rosenthal equation [23,24] for a specific point located on the consecutive track once the laser beam completes the current track. This point may reside either on the current track (solid) or the adjacent powder, depending on the overlapping ratio between the two tracks. Therefore, T_0 is referred to as the next track's temperature and is consistently used throughout this manuscript to distinguish it from the preheat temperature, $T_{preheat}$.

For the sake of simplicity, the Rosenthal equation employs thermophysical properties of solid materials regardless of the scenario. Fig. 2 elucidates the positioning of the examined point relative to the laser beam. This point is situated at the midpoint of the scan length (L/2) and a distance equivalent to the hatch spacing h from the currently scanned track. The return time is defined as $t_r = L/2 \ \nu$ (s). The Rosenthal equation was modified with the respective t_r and h and shown in Eq. (5).

$$T_o = T_{preheat} + \frac{\mathbf{0.3} \times q}{2\pi\lambda[(vt_r)^2 + h^2)]^{\frac{1}{2}}} \times \exp{-v \left[\frac{[(vt_r)^2 + h^2]^{1/2} + vt_r]}{2\alpha} \right]}$$
 (5)

The T_0 obtained from Eq. (5) will be used to calculate the dimensionless beam power q^* in Eq. (1) instead of just simply ambient room temperature of 25 °C. Therefore, the effect of heat accumulation is involved in the LPBF process diagram.

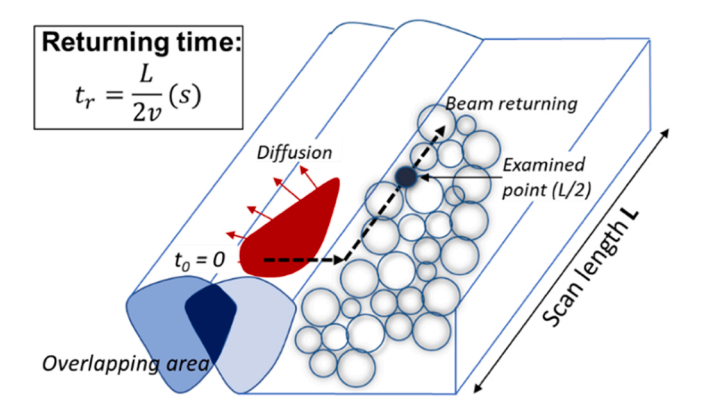


Fig. 2. Illustration showing the determination of returning time with respect to melt pool location and track's length.

1.5. Dimensionless thermal strain factor for evaluating hot cracking susceptibility

Acquisition of the optimal parameters to fabricate a 99% dense part is the first step to achieving sound build quality. However, to make the predictive model to be more versatile, other outcomes should be considered at the same time. One of the critical categories for assessing the printability of metallic materials is hot cracking susceptibility. To predict hot cracking, a strain-rate approach initially proposed by Prokhorov [25] to determine the ductility curve and critical strain rate at which hot cracks initiate was employed and shown in Fig. 3a. In welding, the ductility curve is determined by the Trans-Varestraint weld test [26] in which the maximum crack length was measured for each preset augmented strain, then correlates with the thermal gradient along the weld seam to determine the respective brittle temperature range (BTR) [27]. The critical strain rate over temperature drop $(d\varepsilon_{crit}/dT)$ can be drawn tangent to the ductility curve to determine the critical strain rate (ε_{crit}). In the LPBF process, the strain-rate approach has been applied by several researchers to evaluate the material hot cracking susceptibility [28-30].

To estimate the critical strain rate in the LPBF process, the dimensionless thermal strain factor proposed by Mukherjee et al. [16] was selected due to its capability to be integrated into the diagram. The factor was originally proposed to characterise the dimensional inaccuracy of AM parts caused by thermal distortion, expressed by the equation:

$$\varepsilon^* = \frac{\beta \Delta T}{EI} \frac{t_r}{F \sqrt{\rho}} H^{3/2} \tag{6}$$

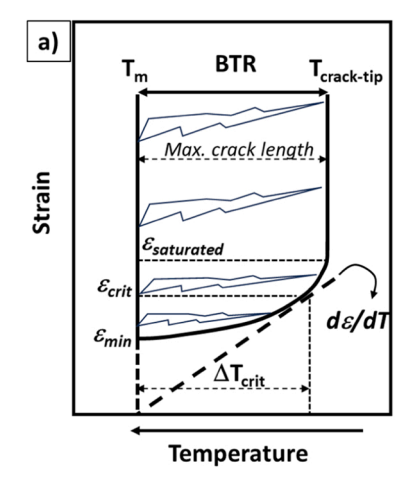
For the second moment of inertia *I*, a partial volume of the base plate where a single layer is deposited on was selected for extracting the rectangular cross-section used for the calculation, as shown in Fig. 3b.

Eq. (6) can be further modified for determining the critical strain rate with respect to the dimensionless beam velocity v^* . The Fourier number F is given by $\alpha \tau / \zeta^2$ where α , τ and ζ are thermal diffusivities, characteristic time and characteristic melt pool length. If we assume the melt pool shape is circular, the characteristic time τ will equal ζ/ν (with $\zeta=2r_B$), thus $F=\alpha/\nu\zeta=\alpha/\nu 2r_B=1/2$ ν^* . Eq. (6) can be re-written as:

$$\varepsilon^* = \frac{\beta \Delta T}{EI} \frac{2v^* t_r}{\sqrt{\rho}} \left(\frac{P}{v}\right)^{3/2} \tag{7}$$

Then, the maximum strain rate was experimentally extrapolated by Mukherjee et al. [16] and can be expressed as a linear function of the dimensionless thermal strain factor:

$$\varepsilon_{\text{max}} = 0.9081\varepsilon^* + 0.0009 \tag{8}$$



Using Eqs. (7) and (8), the maximum thermal strain of individual parameter sets can be obtained and correlated to the material ductility curve to calculate the respective $d\varepsilon/dT$. Values of $d\varepsilon/dT$ are then compared to the critical value of $d\varepsilon_{crit}/dT$ to illustrate the hot cracking tendency of the parameter sets.

2. Validation and evaluation of the process diagram

2.1. Collecting data from the literature and in-house experiments

The normalised LPBF process diagram will be validated against data collected both from the literature and in-house experiments. Despite extensive literature data available for the LPBF process of metallic materials, limited numbers of them can be used. This is due to the incompleteness of the dataset. For example, experimental information needs to include all required parameters and the results should report the measurement of part densities corresponding to the parameters set used. However, most literature data is missing one or some of those critical parameters (e.g., beam diameter) or key parameters are grouped into new variables such as volumetric energy density causing challenges in retrieving information. The in-house experimental results were collected from other studies of researchers working within the same authors' research group. In addition, the process diagram was applied to ABD-900AM Ni-based alloy for parameter selection as the material has no previously published parameters data. All the in-house data satisfy the requirement of completeness. Table 3. lists the literature studies that were used for the data collection.

2.2. Evaluation of the reliability of the LPBF normalised process diagram

Four performance metrics commonly used to evaluate binary classification tasks in the field of machine learning [57] are employed to assess the reliability of the LPBF normalised process diagram in predicting parameters for 99%-dense parts. Table 4 shows a 2×2 confusion matrix constructed for classifications defined by the density data from the prediction of the LPBF process diagram against the actual reported data. In the context of the confusion matrix, density values greater than or equal to 99% are classified as "Positive" while values less than 99% as "Negative". The four categories in the confusion matrix are then defined as follows:

- \bullet True Positives: the diagram correctly predicts "Positive" for data points with a density $\geq 99\%$
- False Positives: the diagram incorrectly predicts "Positive" for data points with a density < 99%

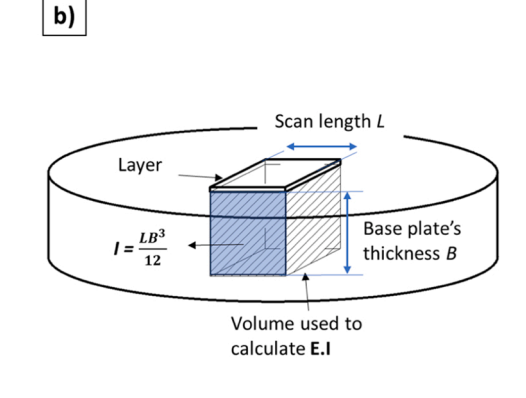


Fig. 3. a) Strain-rate approach using ductility curve to determine the critical strain rate for the threshold of hot cracking initiation (T_m and $T_{crack-tip}$ are liquidus and crack-tip temperatures, respectively); b) A partial volume of the base plate underneath the deposited layer is selected to calculate EI.

Table 3Literature and in-house data for LPBF processing parameters of selected materials.

Cited work	LPBF platform	Alloy system	Process parameters					Thermo-	
			Preheat temperature (°C)	Laser power, P (W)	Scan speed, v (mm/s)	Layer thickness, l (µm)	Hatch spacing, h (µm)	Beam radius, r_B (μ m)	physical properties
Thinh Huynh [31]	SLM 125HL	IN718	None	125 ~ 350	200 ~ 2200	30	120	40	[32]
Georgilas et al. [33]	Renishaw AM250		None	170 ~ 200	461 ~ 600	60	140	35	
In-house	Aconity 3D		None	49 ~ 190	300 ~ 2243.165	30	20 ~ 130	35	
In-house	Aconity 3D	ABD- 900AM	None	95 ~ 360	500 ~ 2310.66	30, 40, 60, 80	50 ~ 140	40	[34]
Adegoke et al. [35]	EOS M290	CM247LC	None	170 ~ 220	2800 ~ 3200	20	20 ~ 40	50	[36]
Vellejo et al. [37]	SLM 125	SS316L	100	$100 \sim 350$	$100\sim2600$	30	120	35	[32]
Pragana et al. [38]	Customised platform		None	245 ~ 270	800	50	50 ~ 100	40	
Leicht et al. [39]	EOS M290		None	195	$800 \sim 1400$	50	60, 90, 120	50	
In-house	Aconity 3D		None	$85 \sim 190$	$300 \sim 1900$	30	40 ~ 100	35	
Yasa et al. [40]	SLM 280	17-4 PH	None	$200 \sim 350$	$600 \sim 1200$	60	90, 120, 150	40	[41]
Bae et al. [42]	SITI-SLM250		None	$180\sim250$	$800 \sim 1100$	40	80	30	
Hu et al. [43]	Self-developed platform		None	200	166.67 ~1666.67	20, 30, 40	90, 110, 130	50	
Promoppatum et al. [44]	EOS M290	Ti-6Al-4 V	None	150	750 ~ 2500	30	100	50	[32]
Dilip et al. [45]	EOS M270		None	50 ~ 195	$500 \sim 1200$	30	100	50	
Kan et al. [46]	EOS M290		None	$160 \sim 300$	$600 \sim 2300$	30, 60	80, 100, 140	50	
Gong et al. [47]	EOS M270		None	40 ~ 160	120 ~ 1560	30	100	50	
Colopi et al. [48]	Customised platform	Cu	None	600 ~ 1000	1000 ~ 3000	50	70, 100	39	[49]
Abdelhafiz et al. [50]	EOS M280		200	$135\sim200$	200 ~ 800	40	50, 80, 100	50	
Bonesso et al. [51]	EOS M280		40	370	200 ~ 500	20	80 ~ 110	41	
Jadhav et al. [19]	In-house platform		300	200 ~ 500	100 ~ 1000	30	90	37.5	
Rebesan et al. [52]	EOS M100	Мо	80	107 ~ 170	750	30, 40	20	20	[53]
Higashi et al. [54]	EOS M290		150	$100 \sim 350$	400 ~ 4000	$20 \sim 60$	70	50	
Gibson and	Renishaw		None	400	$121\sim454$	$50 \sim 100$	30	65	
Lowden [55]	AM400								
Bajaj [56]	Renishaw		200	$143\sim190$	$156 \sim 416$	20, 30	35 ~ 55	25	
	SLM125								

Table 4Confusion matrix for Predicted and Actual data of density for the LPBF process diagram.

Predicted Actual	≥ 99% density (Positive)	< 99% density (Negative)
≥ 99% density (Positive)	True Positives (TP)	False Negatives (FN)
< 99% density (Negative)	False Positives (FP)	True Negatives (TN)

- False Negatives: the diagram incorrectly predicts "Negative" for data points with a density ≥ 99%.
- True Negatives: the diagram correctly predicts "Negative" for data points with a density < 99%.

These categories represent different matchings of predicted and actual data, allowing the evaluation of the model's performance in terms of Accuracy, Precision, Recall, and F1-Score as defined below [57]:

Metrics	Formula	Definition
Accuracy (%)	$\frac{TP + TN}{TP + TN + FP + FN}$	Overall correctness of the model's prediction. This measures how well the model predicts the density of the parts with respect to the melting/vaporisation boundaries

(continued on next column)

(continued)

Metrics	Formula	Definition
Precision (%)	$\frac{TP}{TP + FP}$	The proportion of true positive prediction out of all positive predictions made by the model. This measures how accurately the model predicts good parameters (≥ 99% density)
Recall (%)	$\frac{TP}{TP + FN}$	The proportion of true positive prediction out of all actual positive data points. This measures how well the model predicts bad parameters (< 99% density)
F1-Score (%)	$\frac{2 \times \textit{Precision} \times \textit{Recall}}{\left(2^2 \times \textit{Precision}\right) + \textit{Recall}}$	The F1-score is the harmonic mean of Precision and Recall. The F1-Score assesses the model's ability to make accurate predictions for both good and bad parameters

3. Results and discussion

3.1. The LPBF process diagram versus literature and in-house data of different materials

In this study, a density threshold of 99% was employed to determine whether a set of parameters results in potential keyhole porosities or LOF (lack of fusion) in as-built parts. The boundaries of melting and vaporisation are primarily influenced by the laser beam spot size and layer thickness. These relationships can be expressed using the respective q^*_{net} in Eq. (4), where $z^* = l/r_B$ and $z_0^* = z_0/r_B$ are the two driven

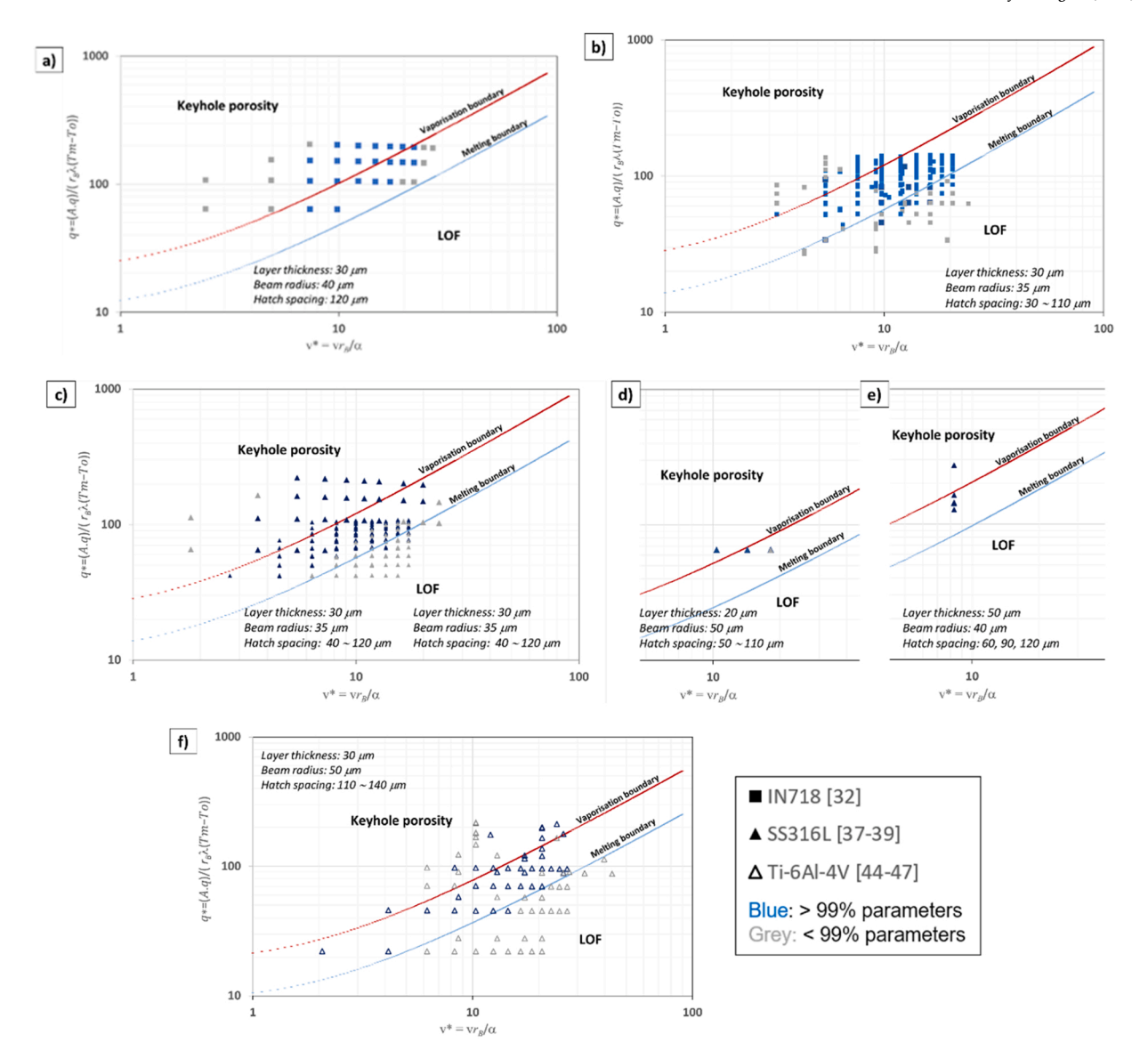


Fig. 4. LPBF process diagram plotting against literature and in-house experiments data for commonly used alloys. Literature data are presented with larger points than in-house experimental data for the case of IN718 and SS316L alloys.

variables. Fig. 4 illustrates the LPBF process diagrams of commonly used commercial alloys using literature and in-house data, as previously listed in Table 2. Good processing parameters resulting in a density $\geq 99\%$ (indicated by blue points) mainly fall within the range defined by the boundaries. Similarly, the parameters' position below the melting boundary matches well with the predicted densities representing for LOF area. However, there are good parameters exceeding the vaporisation boundary yet they are not reported as keyhole porosities, as shown in Fig. 4a and c. This implies a degree of uncertainty within the diagram which is then evaluated in Section 3.3.

3.2. Enhancing data interpretation of the LPBF normalised process diagram

The LPBF normalised process diagram offers a versatile approach for simultaneously considering multiple parameters. However, different combinations of layer thickness and beam radius result in different melting and vaporisation boundaries. Data listed in Table 3 comprises parameters from different sources meaning that numerous diagrams are required to plot all parameters. In addition, this causes challenges when evaluating the reliability of the LPBF process diagram. Therefore, a *q**-

fraction variable is introduced to enhance the data analysis efficiency. To achieve a 99% density, the q^* values must fall within the melting and vaporisation boundaries regardless of layer thickness or beam radius used. Therefore, to determine if the q^* is in the boundaries, the q^* -fraction for a given q^* can be calculated by:

$$q_{fraction}^* = \frac{q^* - q_{melt}^*}{q_{vaporisation}^* - q_{melt}^*}$$

$$\tag{9}$$

The LPBF normalised process diagram plotted with q^* against v^* is now transformed into a diagram of q^* -fraction versus v^* . In this new diagram, data points having a q^* -fraction between 0 and 1 (representing the melting and vaporising boundaries) are considered as good parameters or above 99% density part, depicted by blue colour. Data points that result in below 99% density are represented by grey colour.

It should be noted that a fixed value of $L^*_{m/v} = L_m/[c(T_{m/v} - T_0)] = 0.39$ (dimensionless latent heat of fusion) and $T^* = (T_{m/v} - T_0)/(T_m - T_0) = 1$ or 2 were used to calculate the onset melting and vaporisation boundaries, following the original approach of Ion et al. [8]. However, this has come with certain limitations as different materials may have different latent heat of fusions or vaporising temperatures. For example, Cu has a melting point and vaporising point of 1356 K and 2835 K,

respectively which results in a $T^*_V = 2.365$ instead of $T^*_V = 2$ (taking $T_0 = 273~K$). Therefore, individual material's $L^*_{m/v}$ and values of $T^*_{m/v}$ calculated for each set of parameters were used to improve the LPBF normalise process diagram. All parameters used for processing individual material can now be plotted in the same plot for better comparison and analysis, as shown in Fig. 5.

3.3. The reliability of the LPBF normalised process diagram

Fig. 6 demonstrates the 4-Metrics bar graph for all material data and for individual materials. Overall, the LPBF process diagram achieves approximately 71% for both Accuracy and F1-Score, 65% for Precision and 78% for Recall when considering all material datasets listed in Table 3. The Accuracy and F1-Score indicate a promising evaluation of the LPBF process diagram as it correctly predicts a significant portion of the data that results in either \geq 99% or < 99% density. However, the Precision only achieves up to 65% indicating that it is less reliable for the diagram to predict good parameters.

When considering individual materials, the LPBF diagram demonstrates excellent performance for IN718, SS316L and Ti-6Al-4V alloys of which all four metrics achieve approximately 80%. These are commonly used alloys in the LPBF process meaning good parameter windows have

been well experimented and established. The performance metrics are slightly reduced to approximately 70% when predicting Mo data. However, the metrics for 17–4PH are not as good as other materials, probably due to the smaller dataset size, which was reported to have an influence on the accuracy and robustness in evaluating the performance metrics [58].

It is important to address the case of CM247LC and Cu in Fig. 6 as very high scores are also observed. However, the respective scatter plots in Fig. 5 indicate an imbalanced data distribution for these two materials. The dataset size of CM247LC is small and comprises exclusively of good parameters. Similarly, the dataset of pure-Cu contains only two data points of good parameters despite its large size. This imbalanced data distribution can potentially impact the accuracy when interpreting the data [59]. Therefore, to enhance the predictive capability of the diagram for these two materials, further data collection is necessary.

For ABD-900AM, the process diagram proves to be reliable when being applied for parameter selection. All four metrics achieve a score higher than 75%, indicating that the diagram can be applicable to new materials or uncommon process parameters (various layer thicknesses).

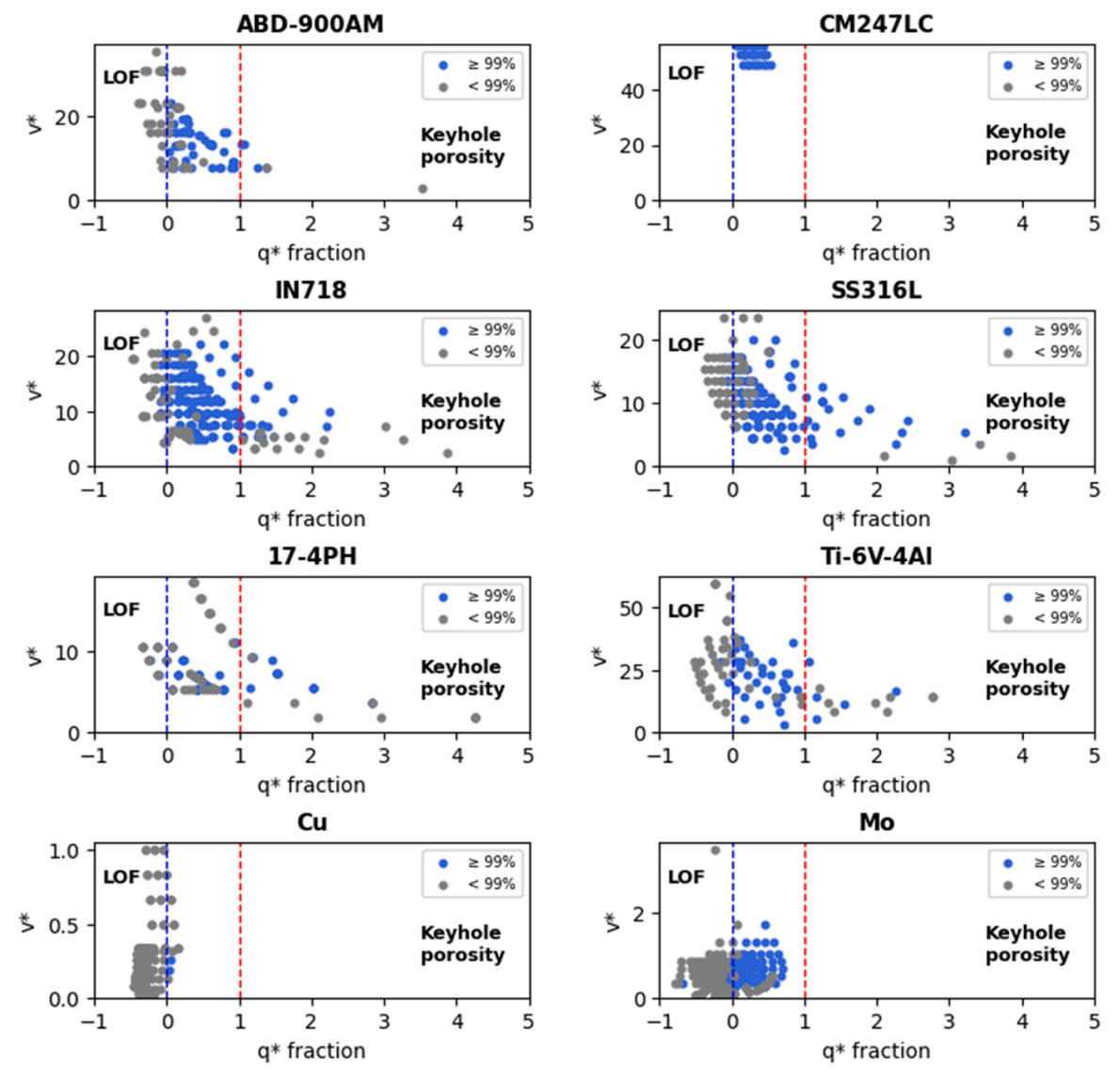


Fig. 5. Scatter plot of materials against q*_fraction using individual material's value of $L^*_{m/v}$ and $T^*_{m/v}$ for vaporisation boundary.

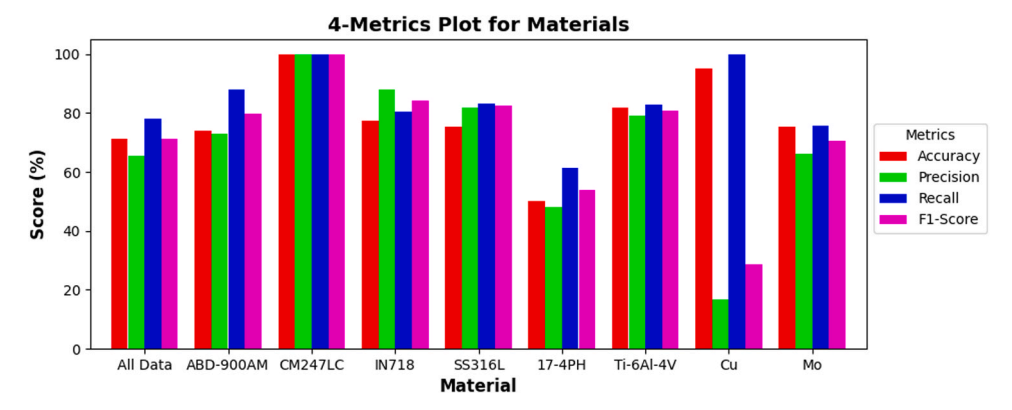


Fig. 6. The performance metrics to evaluate the reliability of the LPBF process diagram in predicting parameters for different materials.

3.4. Expedite the progress in the determination of parameters for the LPBF process

The LPBF process diagram can cover the parameter space of commercially used LPBF platforms with laser power ranging from 25 W to 400 W and a scan speed ranging from 100 mm/s to 7000 mm/s. To determine the optimal process window for a particular material without previously published data, the Design of Experiment (DOE) approach is normally employed. This involves investigating the effects of two or more key parameters and statistically analysing their impact on desired outcomes, such as part density, crack density, or surface roughness. Depending on the number of studied factors and outcomes, the number of fabricated samples can be exponentially increased. The procedure begins with a comprehensive design study covering the LPBF machine parameter space. This process is reiterated multiple times to progressively narrow down the process windows until the optimal parameter space is found, as illustrated in Fig. 7a. Consequently, this approach requires substantial resources, including time, materials and labour costs.

With the aid of the LPBF process diagram, the determination of the optimal process windows can be quick and simple. This diagram allows the examination of multiple parameters against various desired outcomes simultaneously and discernibly. For example, parameters required for higher build rates are located in the upper-right corner of the diagram (high $q^* - v^*$). When the processing region has been identified, a DOE can be then established considering a specific processing window to fall within the good processing range for 99% density, as illustrated in Fig. 7a. Furthermore, the critical strain rate over temperature drop $d\varepsilon/dT$ can be calculated to assess the sample cracking

susceptibility. Varying parameters such as layer thickness or beam spot size can also be evaluated by the diagram, as depicted in Fig. 7b, c. The prerequisite requirements are to define the material thermophysical properties so that calculations for vaporisation and melting boundaries can be proceeded.

4. Application of the lpbf process diagram on CM247LC Ni-based allov

4.1. Experimental procedure

4.1.1. LPBF fabrication of CM247LC alloys samples

After validation using the literature data and in-house data, the normalised LPBF process diagram was applied to the legacy CM247LC high- γ ' Ni-based alloy for further confirmation of its capability in parameter selection for high-density and low-cracking built parts.

An Aconity Lab LPBF machine manufactured by Aconity3D GmbH, Germany was used for the fabrication of the samples. The machine is equipped with a 1070 nm wavelength fibre laser at a maximum power of 400 W. However, the power was limited to 390 W for safer operational conditions. The laser beam can be focused down to a minimum of 70 μm spot size using an F-theta lens optical system. The Aconity Lab has a cylindrical build envelope of Ø170 mm \times 200 mm in height.

The CM247LC gas-atomised powders were supplied by Carpenter Additive, with a powder size distribution ranging from 15 \sim 53 μm . Four DOEs with a total of 52 cubes (10 mm \times 10 mm x 5 mm) were built with parameter sets spanning across the machine processing windows. Central composite design (CCD) was also applied to acquire the parameters of the DOEs. DOE 1 is a group of parameters of low P and v; DOE 2 is a

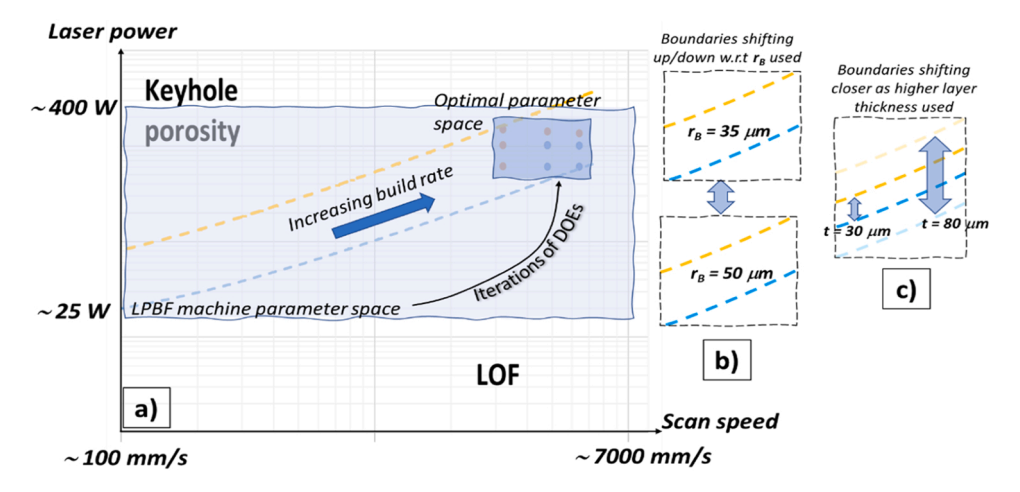


Fig. 7. The versatility of the LPBF diagram as compared to the conventional DOE approach: a) The optimal parameter space can be defined quickly and simply; b) and c) The effect of beam spot size and layer thickness on the keyhole and melting boundaries, respectively.

group of high P – medium v; DOE 3 and DOE 4 use the same P and v, and are classified as high P – v groups, as shown in Fig. 8. For DOE 1, 2 and 3, a standard scanning strategy with 70 μ m hatch spacing and 90° rotations in every layer was employed. This means that individual scans will have a constant scan length of 10 mm. For DOE 4, a stripe scanning strategy with a stripe width of 5 mm was used. In addition, hatch spacing was reduced to 35 μ m. This aims to reduce the return time and enhance the track-by-track heat accumulation which increases the next track's temperature T_0 . According to Eq. (7), ε^* will be reduced as the deposition time t (i.e., return time) and ΔT are reduced. In other words, reducing the scan length and increasing T_0 will alleviate the hot cracking susceptibility. Fig. 8 illustrates the LPBF normalised process diagram constructed for DOEs of CM247LC with the integrated estimation of values of $d\varepsilon/dT$.

The brittle temperature range (BTR) against the augmented strain (%) curve of CM247LC was determined by Chun et al. [60]. Based on this curve, the critical strain rate over temperature drop $d\varepsilon_{crit}/dT=(\varepsilon_{crit}-0)/\Delta T_{crit}$ can be determined to be ${\bf 2.1}\times 10^{-5}$ %/K, following the method depicted in Fig. 3a, and this is the critical strain rate threshold (CST) for evaluation of hot cracking susceptibility of the parameters used. Calculated values of $d\varepsilon/dT$ for CM247LC samples were obtained using Eqs. (6)–(8). Table 5 lists details of the parameters selected for the experiments.

It should be noted that DOE 3 and DOE 4 were processed with relatively high scan speeds (2615.5 \sim 5232 mm/s). Thus, a lower

surface absorptivity A = 0.2 was assumed for DOE 3 and DOE 4, instead of A = 0.3 as being used in DOE 1 and DOE 2. Higher scan speeds were reported to result in lower surface absorptivity [17]. Khorasani et al. [61] showed that surface absorptivity in LPBF of IN718 alloy reduces as the ratio between laser power/scan speed (i.e., line energy) reduces. This can be attributed to the interaction of the incident laser beam and the vapour plumes and spatters released during the melt pool formation [62–64]. Zheng et al. [63] noted that varying scanning speeds at constant laser power (400 W) led to distinct outcomes: low speeds (200 mm/s) induced melt pool instability and significant spatter production, medium speeds (400-500 mm/s) suppressed spatter formation through inclined vapour plumes, and high speeds (1000-2000 mm/s) resulted in both intensive spatters and vapour plumes ejected opposite to the scanning direction. In laser welding, the vapour plumes cause an attenuation effect of up to 40% to the laser energy absorption [65,66], potentially resulting in instability of the melt pool and tending to increase the defect formation such as lack of fusion [62].

4.1.2. Measurement of part density and crack density

Samples were removed from the base plate by wire electrical discharge machining (wire EDM). The cubic samples were sectioned along the building direction for cross-sectional characterisation. The samples were then passed through a standard metallurgical preparation procedure of mounting, 4-step grinding (240, 800, 1200 and 2500 grit papers) and 2-step polishing (3 μ m diamond suspension, then 0.5 μ m

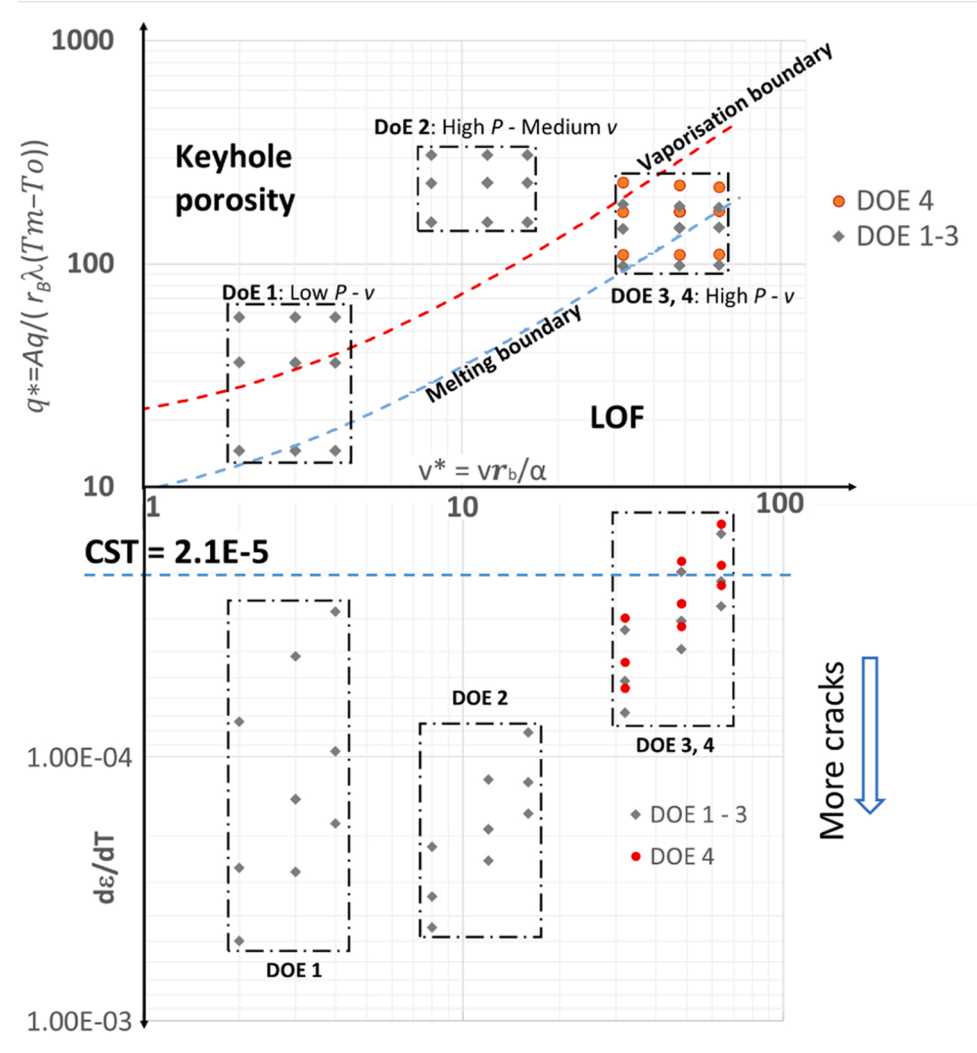


Fig. 8. LPBF process diagram of three DOEs for CM247LC alloy with the prediction of part density and hot cracking density.

Table 5Details of parameters used in the fabrication of CM247LC samples.

Material	Laser power, P (W)	Scan speed, v (mm/s)	Hatch spacing, h (μm)	Layer thickness, l (μm)	Beam radius, r_B (μ m)	Scan length, <i>L</i> (mm)	q *	v *	dε/dT (10 ⁻⁵ %/K)
CM247LC – DOE 1	23.5 ~ 89	163.42 ~ 326.85	70	20	35	10	14.55 ~ 57.66	2 ~ 4	2.81 ~ 49.9
CM247LC – DOE 2	217 ~ 386	653.71 ~ 1307.43	70	20	35	10	153.83 ~ 307.5	8 ~ 16	8.1 ~ 44.4
CM247LC – DOE 3 ^a	190 ~ 390	2615.5 ~ 5232	70	20	35	10	97.95 ~ 181.38	32 ~ 64	1.43 ~ 6.81
CM247LC – DOE 4 ^a	190 ~ 390	2615.5 ~ 5232	35	20	35	5	109.81 ~ 231.65	32 ~ 64	1.3 ~ 5.49

^a DOE 3 and DOE 4 used a laser absorptivity of 0.2; DOE 1 and DOE 2 used a laser absorptivity of 0.3.

colloidal silica) prior to imaging by optical microscopy and scanning electron microscopy (SEM).

An Olympus BX51 optical microscopy equipped with Clemex image processing software was used for capturing images of polished samples at magnifications of 100X. The images were then analysed for porosity and crack density using the ImageJ software. For porosity density measurement, the images were converted to 8-bit black and white images then an automatic threshold was applied to distinguish porosities (black) from the solid material (white). For crack detection and crack density measurement, similar 8-bit converting and thresholding were applied; then the "Ridge Detection" plug-in was employed with an application of circular index ranging from 0 to 0.65 to remove lack of fusion and porosity defects. For characterisation of the cracking mechanism, a field-emission Inspect F scanning electron microscope was employed to capture high-magnification images of crack surfaces.

4.1.3. Near-infrared thermal imaging

The Aconity Lab machine is equipped with an internally developed thermal camera monitoring system. The field of view (FOV) was set to 15 degrees with respect to the building direction, effectively covering a $70 \times 70 \text{ mm}^2$ observation area of the build plate. To capture thermal images of the processing layers, a periscope lens consisting of six optical elements was integrated into the build chamber. The lens was then connected to a Hamamatsu C11440-42U30 CMOS camera positioned outside the chamber. The camera has a resolution of 2048 ×2048 pixels, perfectly matching the 70 ×70 mm² observation area. This configuration enables the capture of 100 frames per second. A band pass filter (Thorlabs FL905 - 10) was used to restrict the wavelength band to 905 nm, featuring a full-width-half maximum of 10 nm. Additionally, a neutral density (ND) filter (Thorlabs NENIR510B) with optical density (OD) 1.0 was used to attenuate the radiance. To prevent any intense laser radiation from reaching the sensor, a short pass filter (Thorlabs FESH1000) was strategically implemented.

The calibration of the camera involved employing a black body furnace encompassing temperatures ranging from 900°C to 1500°C . The maximum temperature capacity was ascertained to be 1689°C for a theoretically perfect blackbody, considering the camera's dynamic range. Furthermore, emissivity measurements were conducted on mirror-like polished CM247LC samples, yielding a value of 0.1594. Upon factoring in this emissivity correction, the camera became capable of accurately measuring temperatures up to a maximum of 2300°C .

4.2. Result and discussion

4.2.1. Density and crack density maps of the DOEs

Samples from DOE 1 to DOE 3 were characterised by scanning electron microscopy (SEM) to confirm that hot cracking was the main mechanism. The characterisation of cracks' surfaces reveals evidence of dendritic morphology, indicative of solidification cracking. Additionally, liquation cracking was evidenced by smooth and wavy surfaces of grain boundary cracks. Detailed SEM images are provided in Appendix B.

Figs. 9 and 10 display the density and crack density map of the four DOEs conducted for CM247LC using the LPBF normalised process diagram for parameter selection. The processing window of each DOE is depicted against the melting and vaporisation boundaries, along with the measured density of the samples. Colour-coded regions showing LOF (blue), 99% density (green) and keyhole porosity (yellow) are also superimposed. In addition, the respective crack density map is plotted for all the samples with respect to the estimated strain rate over temperature drop $d\varepsilon/dT$. Additionally, colour-coded regions are superimposed on the plot, indicating LOF (blue), 99% density (green), and keyhole porosity (yellow).

The DOE 1 process window comprises parameters at low laser powers (*P*) and scan speeds (*v*), spanning vertically from LOF to keyhole porosity regions. The diagram not only predicts the 99%-dense parameters but also highlights the corresponding defects. Optical images of samples 3, 9 and 12 captured with keyhole porosity are shown in Fig. 9a. Conversely, the insufficient energy input of samples 2, 7 and 13 results in failed builds. Keyhole porosity samples are also observed with the highest crack density, as depicted in Fig. 9b. The initiation of keyhole pores appeared to be a favoured site for hot cracks to form. In contrast, pre-existing hot cracks can release trapped gas pores during remelting of the successive scans [67].

In DOE 2, the extremely high energy inputs not only created hot cracks but also extensive hot tears. The term "hot tears" is to describe the more severe hot cracks that form cavity-like features which are substantially larger than normal hot cracks, as indicated in Fig. 9c and d. The measured cracking density ranges from 1.6 to 3.84 mm/mm². However, it is noteworthy that keyhole porosity is observed to be minimal in most samples produced during DOE 2, except for samples 3 and 12. The OM images in Fig. 9c and d reveal bundles of hot cracks surrounding and interconnecting with the hot tears. Furthermore, the size and severity of the hot tears exceed those of the keyhole pores, suggesting that the formation of hot tears could have deleterious effects on the keyhole pores. Scanning electron microscopic (SEM) images showing evidence of the interactions between hot tears, hot cracks, and keyhole pores were provided in Appendix B. In the literature, advanced characterisation techniques such as in-situ X-ray imaging [67,68] should be employed to delve deeper into this interaction. Kouraytem et al. [67] observed, that through dynamic X-ray radiography, successive laser scans release gas bubbles from existing hot cracks formed in preceding tracks. While the authors did not elaborate further on this interaction, the gas bubbles may exacerbate the hot cracks, leading to the formation of hot tears.

DOE 3 and DOE 4 were processed with the same P and ν , but with different scan lengths (i.e., 10 mm and 5 mm, respectively). In DOE 3, samples processed (e.g., samples 1, 5, 9 and 13) with parameters below the melting boundary are observed with a great extent of porosity, as illustrated by OM images in Fig. 10a. However, by reducing the scan length from 10 mm to 5 mm, part density can be improved significantly. For example, the density of samples 5 and 9 is only 68.5% and 88.8% in DOE 3 increasing to 94.2% and 98.4% density in DOE 4, as shown in Fig. 10c. The crack density was significantly reduced in DOE 3 compared

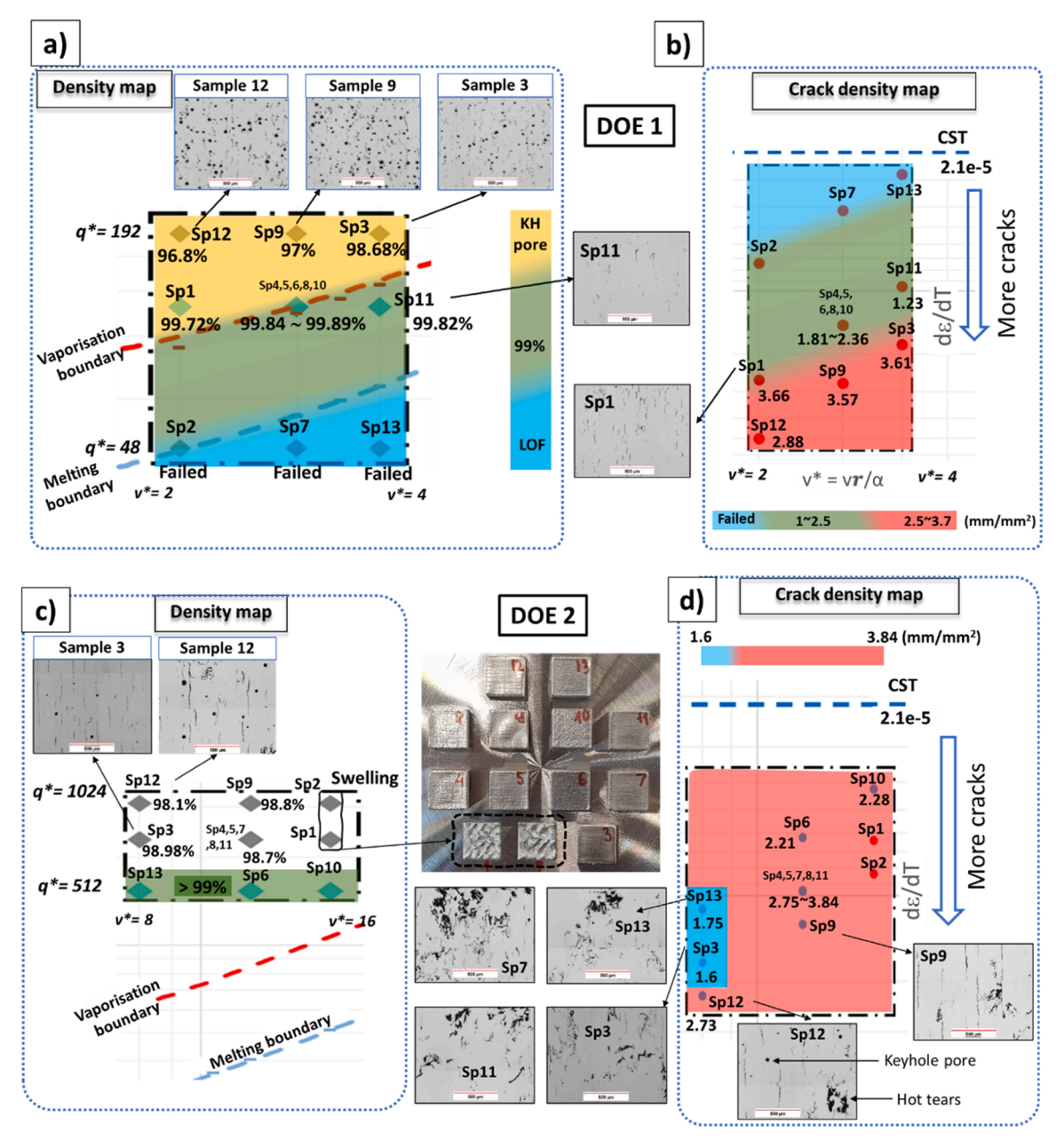


Fig. 9. Sample density and cracking density maps of CM247LC: (a, b). DOE 1 and (c, d). DOE 2.

to DOE 1 and DOE 2. While crack densities in DOE 1 and DOE 2 could be as high as 3.7–3.84 mm/mm², samples in DOE 3 exhibited crack densities ranging from 1.9 to 2.6 mm/mm². This indicates that crack density reduces following the reducing thermal strains predicted by the LPBF process diagram. By shortening the scan length in DOE 4, the crack density was further reduced to a range of 0.29–1.8 mm/mm², as shown in Fig. 10d. This shows a considerable decrease in crack density considering the comparatively minor reduction in predicted $d\epsilon/dT$ observed in DOE 4 in contrast to DOE 3. The following Section 4.2 will elucidate this observation using thermal imaging of selected samples from DOE 3 and DOE 4.

Fig. 11 shows the OM images taken of several samples in DOE 4 with very few cracks that can be observed, except for sample 11. As in Fig. 10c, only samples 10 and 11 were observed with higher crack densities of 1.2 and $1.82 \, \text{mm/mm}^2$, respectively. However, cracks in these two samples are mainly observed near the edges where the laser beam turns over for the successive scan tracks, causing increasing in heat accumulation at the turning points and thus potentially increasing the

thermal strains. Nevertheless, DOE 4 demonstrated that the LPBF normalised process diagram incorporated with the thermal strain factor can be an effective approach to achieving high-density and low-cracking built parts.

4.2.2. Effect of returning time and hatch spacing on the local temperature and hot cracking in LPBF of CM247LC

The hot cracking susceptibility in this study was evaluated based on the $d\varepsilon/dT$, primarily defined by the thermal strain factor ε^* and ε_{crit} in Eqs. (7) and (8), respectively. Values of $d\varepsilon/dT$ for all samples of DOE 1 and DOE 2 presented in Table 5 are above the critical strain threshold of 2.1×10^{-5} %/K, corresponding to their high crack density measurements (1.6–3.84 mm/mm²). Appropriate tuning of several key factors resulted in decreasing crack density in DOE 3 and DOE 4. These factors can be identified from Eq. (7) such as ΔT , t, v^* and P/v. An optimised line energy P/v is crucial to achieve 99%-part density and is dependent on the beam diameter and layer thickness used. P/v also has the most significant impact on the thermal strain, as shown in Eq. (7). Changing v^*

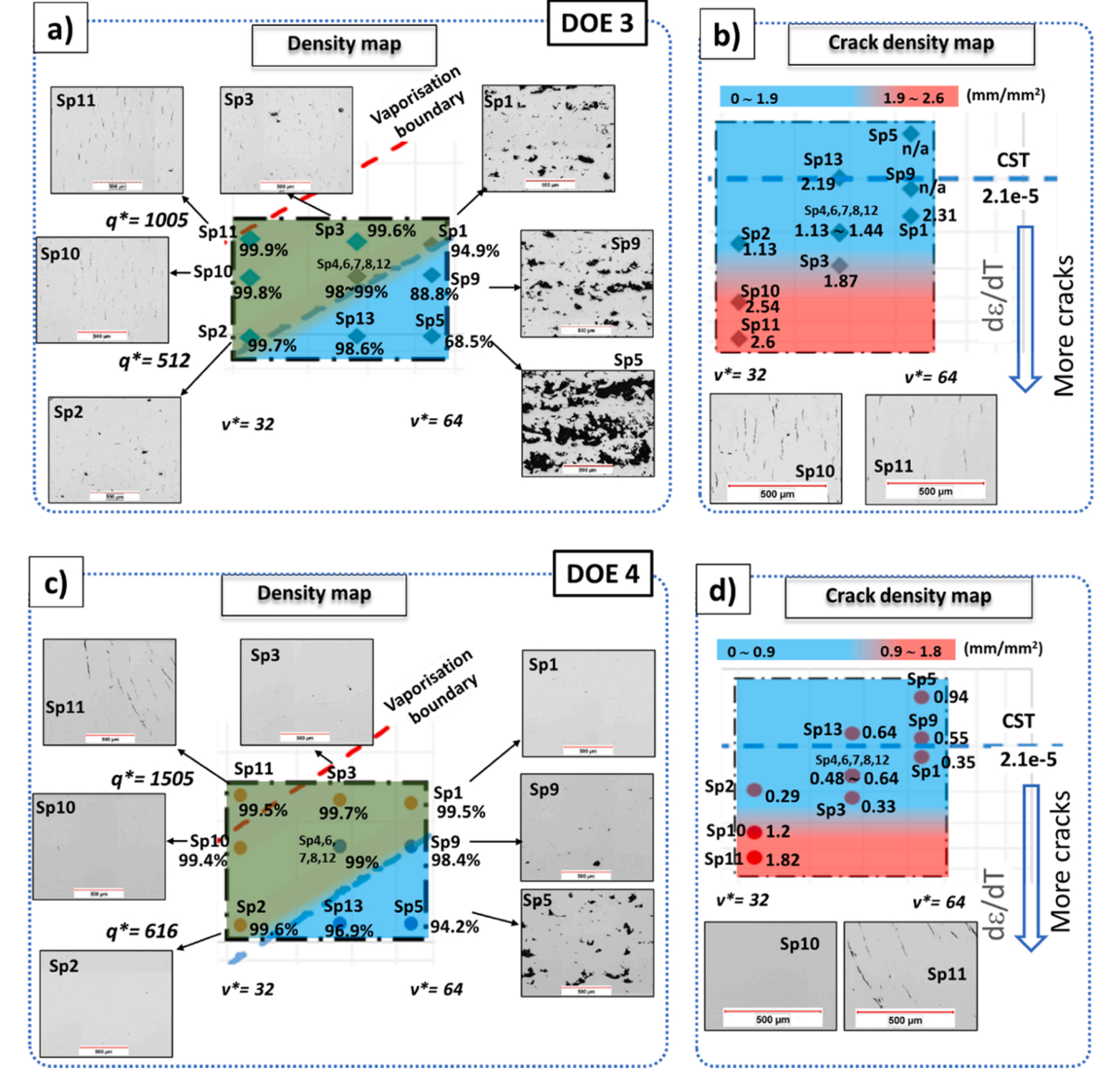


Fig. 10. Sample density and cracking density maps of CM247LC: (a, b). DOE 3 and (c, d). DOE 4.

simultaneously and inversely changing the returning time t, consequently, these two factors counterbalance each other, resulting in a less pronounced effect on $d\epsilon/dT$. To this point, the remaining factor, ΔT , will be the key element to reducing the hot cracking susceptibility. While the material melting point T_m is fixed, increasing T_0 will therefore help to reduce ΔT . This can be done by simply reducing the scan length to increase the heat accumulation effect. In addition, shorter scan lengths result in faster heat source returning time (without changing ν^*), thus even further reducing $d\epsilon/dT$.

The effect of key factors can be better illustrated by Fig. 12, where literature studies on LPBF of CM247LC are compared with DOE 4 in terms of density and crack density, as estimated by the LPBF normalise process diagram. Carter [69] reported extensive solidification cracking with a density ranging from 1 to 10 mm/mm^2 in his study on LPBF of CM247LC. Adegoke et al. [35] achieved high density with less or crack-free CM247LC samples. The parameters used in the two studies are plotted on the LPBF process diagram, aligning well with the processing range conducive to the 99%-density part, as depicted in Fig. 12a and b. Hot cracking susceptibility was accurately predicted as the diagram shows a notable correlation between crack density and the estimated $d\epsilon/dT$ values in Fig. 12c, incorporating data from [35,69], and

our DOE 4. In Carter's work [69], P/v values were sufficient to achieve highly dense samples but not well optimised for low crack density although a 5-mm scan length was used. In contrast, Adegoke et al. [35] well optimised their parameters. The good P/v selection incorporating 2.5-mm stripe scanning resulted in not only high-density parts but also low $d\varepsilon/dT$ values as they are mostly lower than the critical threshold.

To provide insight into the rising T_0 due to shorter scan length, thermal images of samples with the highest energy input of DOE 3 and DOE 4 are specifically selected and shown in Fig. 13a and b, respectively. At first glance, the melt pool dimensions of each sample with respect to the scan length can be observed differently. In DOE 3, the melt pool length is much shorter than the track length (10 mm) while in DOE 4, the melt pool length captured is almost equal to the track length (5 mm). The temperature T_0 was measured along the centre line of the next track, following the deposition direction of each sample. The data on T_0 and thermal gradients can be then extracted.

The actual T_0 values measured at the next track's mid-point by the thermal camera are approximately 845 °C and 1400 °C for samples 11 of DOE 3 and DOE4. These are much higher than the calculated values of 215.7 °C and 451.7 °C by Rosenthal's equation, respectively. This can be understandable as the actual heat transfer and accumulation during the

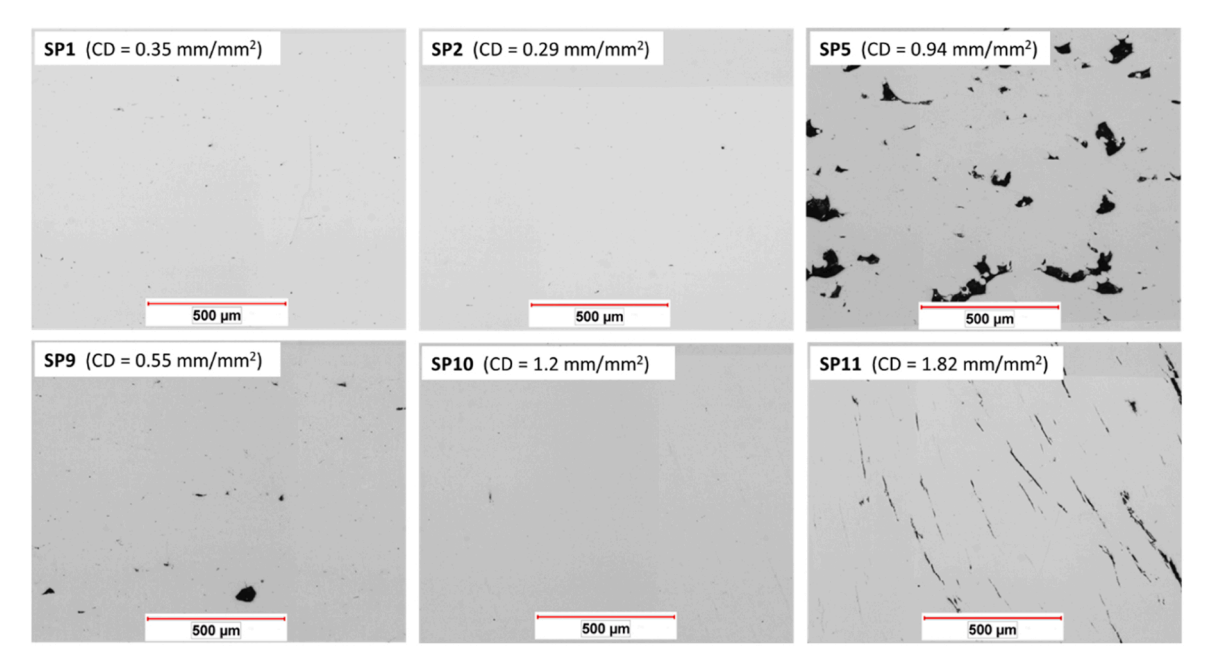


Fig. 11. OM images of selected samples in DOE 4 with crack density (CD) measurements.

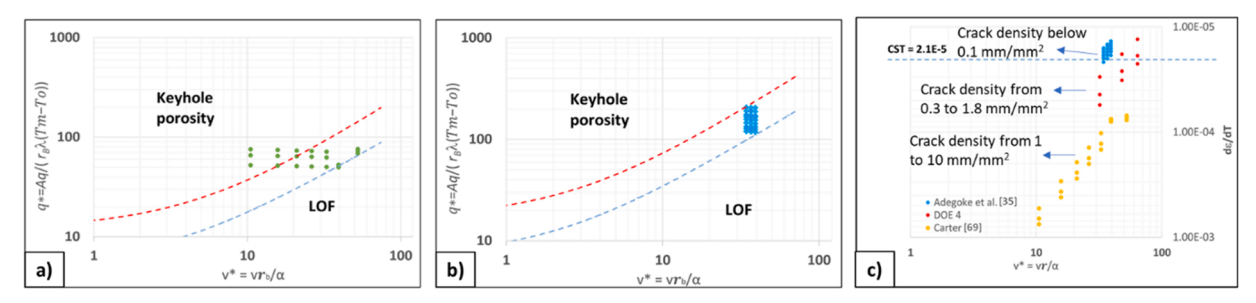


Fig. 12. a) Plots of data from the work of Carter [69]; b) Plots of data from the work of Adegoke et al. [35]; and c) Crack density comparison against the estimated $d\epsilon/dT$.

build cannot be resolved by simply analysing Rosenthal's equation. The 10 mm scan length of DOE 3 results in a very steep thermal gradient of 121 °C/mm (Fig. 13c) as compared to a near plateau thermal gradient observed in DOE 4 when a 5 mm scan length was used (Fig. 13d). This low thermal gradient, meaning low in ΔT , elucidates the reason for lower cracking densities measured in DOE 4 samples despite a slight reduction in estimated values of de/dT as compared to DOE 3.

4.2.3. Limitation and potential improvement of the normalised LPBF process diagram

The normalised LPBF process diagram has shown a simple but considerably accurate and reliable approach to predicting parameters for 99% density-built parts. However, the simplicity of the approach comes with several approximations, which introduce certain limitations that affect the diagram's overall performance. One such limitation is the selection of material thermo-physical properties at room temperature and their subsequent treatment as constant throughout the analysis. This assumption can lead to discrepancies in the accuracy of the predictions.

The mathematical temperature field employed to develop the LPBF process diagram is solely derived for the conduction melting regime [8], without accounting for the keyhole melting mode. The on-set vaporisation boundary is determined based on the peak temperature at the melting depth z^* required to reach the boiling temperature, as mentioned in Section 1.3. Therefore, energy input (i.e., q^*) exceeding this boundary does not necessarily assure the formation of keyhole porosity. In LPBF practice, keyhole pores may not form even when

keyhole melt pools are observed [31,37]. It is noteworthy that the keyhole melting may be undesirable from the perspective of LPBF process optimisation due to its instability, higher defect propensity and increased energy consumption. Therefore, the normalised LPBF process diagram primarily focuses on the conduction mode melting, resulting in a more reliable parameter selection in this regime.

The laser absorptivity strongly influences the calculation of dimensionless numbers such as q^* and T_0 . Variation of the laser absorptivity is more sensitive in high scan speed regions, as observed in the DOE 4 of the CM247LC case study. In addition, laser absorptivity depends on different melting modes, powder layer thickness or beam spot sizes.

For the thermal strain factor, the determination of the critical strain rate over temperature drop $d\varepsilon/dT$ is very limited in the literature. For materials with high hot cracking susceptibility, existing $d\varepsilon/dT$ values are normally measured by bead-on-plate weldments on as-cast base materials [60,70-72]. Hot cracking includes solidification and liquation cracking within the weld fusion zone and partially melted zone (PMZ), respectively [73]. While the microstructure of the fusion zone closely resembles that of parts fabricated by LPBF, the as-cast microstructure of PMZ tends to be significantly coarser [73]. Such differences can impact the evaluation of hot cracking susceptibility and lead to reduced accuracy when adapting the $d\varepsilon/dT$ parameter to the normalised LPBF process diagram.

The melting and vaporisation boundaries of the normalised LPBF process diagram are determined by a pre-defined dimensionless depth $z^* = l/r_B$. Theoretically, the melting of one layer is sufficient to create a

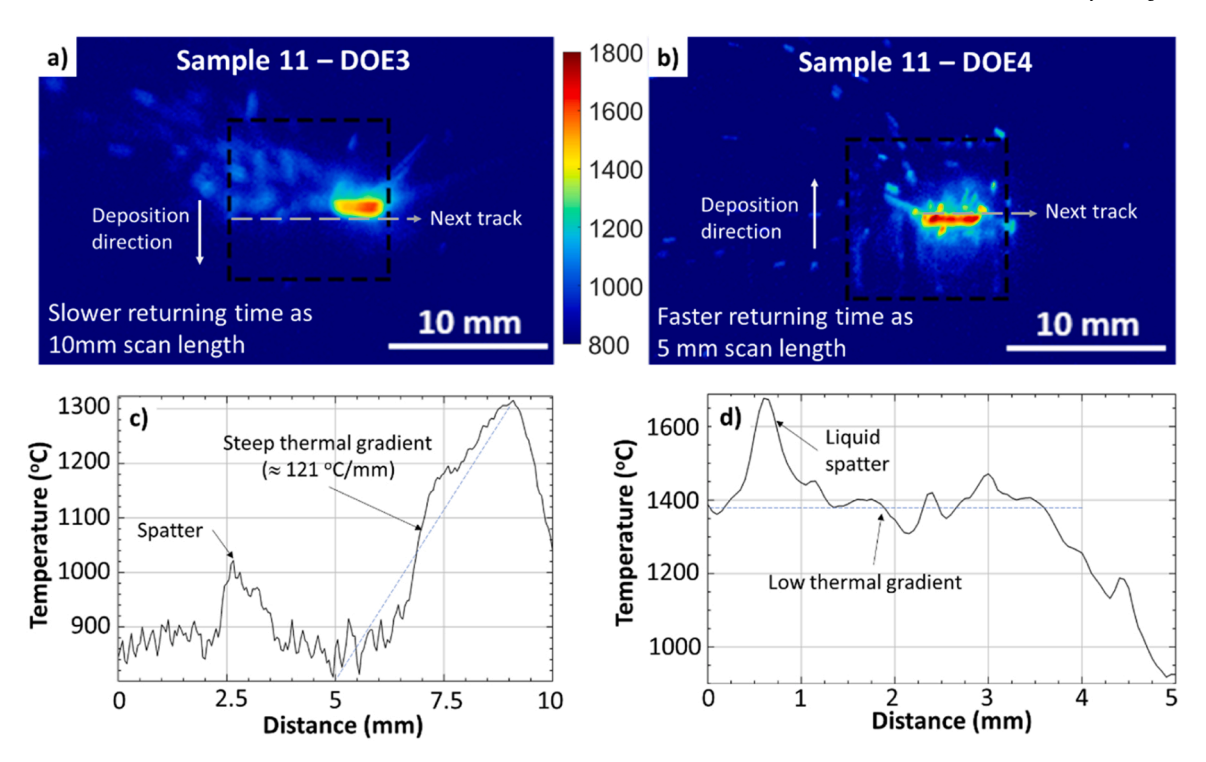


Fig. 13. Effect of return time on the next track's temperature T₀. The cubic sample is illustrated by the black dashed square. The next track of each sample used for extracting the thermal gradient in both DOEs are highlighted. Steep thermal gradient is observed in DOE 3 while a plateau thermal gradient is observed in DOE 4.

bond between consecutive layers. However, in practice, the actual melt depths should exceed the layer thickness, especially for materials with high thermal conductivities like copper. This can enhance the performance of the LPBF process diagram. In Fig. 14, the vaporisation boundary is kept unchanged whilst the melting boundary is shifted upward by adjusting the dimensionless depth to be 1.2 times of layer thickness, thus refining the good processing range.

To enhance the normalised LPBF process diagram further, additional measurements or studies could be pursued. However, such efforts may come at a cost, potentially compromising speed for accuracy, and complicating the diagram construction. For instance, a thermal monitoring system could be implemented for the in-situ measurements of T_0 , enabling the real-time calculation of q^* , v^* , and $d\varepsilon/dT$ using temperature-dependent thermo-physical properties. In this way, a closed-loop feedback integration into analytical equations can be established, ensuring consistent heat accumulation/distribution throughout the laver-by-laver building process.

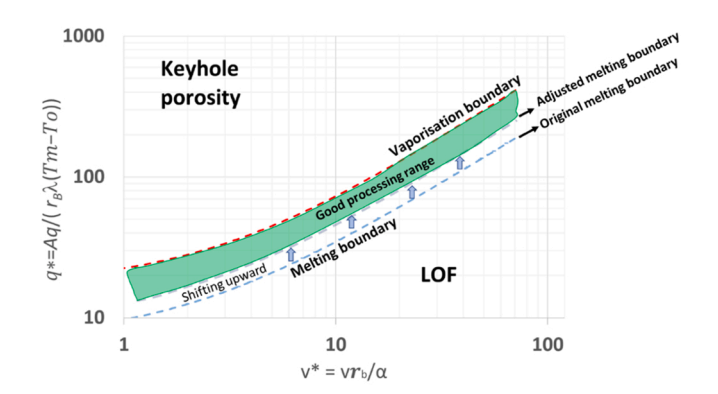


Fig. 14. Enhancement of the LPBF process diagram by increasing the predefined dimensionless depth z^{\star} .

5. Conclusion

In this study, the well-established dimensionless numbers used for the laser welding process diagram have been adapted for the laser powder bed fusion process (LPBF). This adaption considered specific processing characteristics such as scan length, hatch spacing, and powder layer thickness. The capability of the LPBF normalised process diagram was scrutinised through a comprehensive analysis of existing literature and in-house experimental data, showing high reliability in predicting parameters resulting in 99%-density as-fabricated parts. Furthermore, the dimensionless thermal strain factor incorporated with the material brittle temperature range (BTR) was integrated into the diagram, providing an effective way to assess the hot cracking susceptibility of the selected parameters. The applicability of the LPBF normalised process diagram was demonstrated by a case study using the CM247LC Ni-based alloy. The outcomes indicate the promise and reliability of this approach to expedite the parameter design process. Below are the specific findings:

- The LPBF process diagram demonstrates high reliability and accuracy, achieving up to 80% in the prediction of parameters associated with lack of fusion, 99% density and potential keyhole porosity. This applies to commonly used materials such as IN718, SS316L and Ti-6Al-4V alloys and pure Mo.
- Application of the LPBF process diagram to determine the optimal parameters for ABD-900AM alloy achieved up to 75% accuracy even under varying layer thickness conditions.
- 3. The LPBF process diagram provides a robust and interactive tool for the evaluation of parameters regarding their prospective outcomes such as 99%-density and potential defects including lack of fusion, keyhole porosity or hot cracking.
- Application of the LPBF process diagram to CM247LC alloy showed that hot cracking susceptibility can be estimated by the thermal strain factor for the selected parameters.
- 5. The reduction of scan length and hatch spacing showed a positive impact on mitigating hot cracking susceptibility, providing that

appropriate laser powers and scan speeds were selected. Shorter scan lengths were observed to enhance the local heat accumulation, thus lowering the thermal gradient, as confirmed by thermal imaging. Consequently, an increase in part density and a decrease in crack density were achieved.

6. The LPBF process diagram facilitates the simultaneous and reliable evaluation of multiple key parameters of the LPBF process (e.g., laser power, scan speed, scan length, hatch spacing, layer thickness or beam spot size) against various outputs (e.g., density, cracking, build rate). This expedites the optimisation process, leading to considerable savings in material and labour costs.

CRediT authorship contribution statement

Minh Anh Luan Phan: Writing – review & editing, Writing – original draft, Validation, Software, Methodology, Investigation, Formal analysis, Data curation, Conceptualization. Oliver Dew: Methodology, Data curation. Iain Todd: Writing – review & editing, Supervision, Investigation, Funding acquisition, Formal analysis, Conceptualization.

Declaration of Competing Interest

The authors declare that they have no known competing financial interests or personal relationships that could have appeared to influence the work reported in this paper.

Data availability

Data will be made available on request.

Acknowledgements

This work was supported by EPSRC MAPP Grant EP/P006566/1. The authors wish to acknowledge support from the Henry Royce Institute for Advanced Materials, funded through EPSRC Grants EP/R00661X/1 for access to the Aconity Lab at The University of Sheffield. We would like to thank Dr Yufeng Lai for his support in the processing of thermal imaging data.

Appendix A. Construction of the LPBF normalised process diagram

In this section, summary on the construction of the LPBF normalised process diagram is demonstrated. For more detailed steps, we advised readers to refer to the original works [8,21]. For a heating and melting mode, a mathematical model for the temperature field for a Gaussian laser beam was proposed to define the peak surface temperature. This model can also be used to predict the welding surface treatment or melting depths. The mathematical model is expressed by:

$$T - T_o = \frac{Aq}{2\pi \lambda v [t(t+t_0)]^{\frac{1}{2}}} \times exp - \frac{1}{4\alpha} \left| \frac{(z+z_0)^2}{t} \right|$$
(A.1)

Eq. A.1 can be re-expressed in dimensionless terms using the dimensionless beam power q^* and velocity v^* defined in Eqs. 1 and 2. The temperature field is shown by Eq. 3′, as:

$$T^* = \frac{(T - T_0)}{(T_m - T_0)} = \frac{\left(\frac{2}{\pi}\right) \times \left(\frac{q^*}{v^*}\right)}{\left[t^*(t^* + 1)\right]^{\frac{1}{2}}} \times \exp\left[\frac{\left(z^* + z_0^*\right)^2}{t^*}\right] \tag{3'}$$

To determine the z_0^* , the normalised time to peak temperature t_p^* at a given depth must be found. This can be done by differentiating Eq. 3' with respect to time and solving the resulting quadratic equation:

$$t_p^* = \frac{1}{4} \left\{ 2(z^* + z_0^*)^2 - 1 + \left[4(z^* + z_0^*)^4 + 12(z^* + z_0^*)^2 + 1 \right]^{\frac{1}{2}} \right\}$$
(A.2)

Next, t_p^* is substituted into Eq. 3' to yield the normalised peak temperature T_{P}^* . This T_{P}^* is then equated to a solution for the peak temperature at surface ($z^* = 0$) produced by a stationary beam during a beam interaction time ($2r_B/\nu$). The dimensionless term for this solution is:

$$(T_p^*)_{z^*=0} = (1/\pi)^{3/2} q^* \tan^{-1} (8/\nu^*)^{1/2}$$
(A.3)

In summary, the equation Eq. 3' is set equal to A.3 with $t^* = t_p^*$ and considered at $z^* = 0$, yielding:

$$e^{\frac{-2t_p^*+1}{t_p^*+1}} = \left[\frac{v^*.\tan^{-1}(\sqrt{\frac{8}{v^*}})}{2\sqrt{\pi}} \right]^2 [t_p^*(t_p^*+1)]$$
(A.4)

At this stage, z_0^* can be seen only dependent on v^* but it cannot be explicitly expressed as a function of v^* . To solve for z_0^* , its value must be incremented until the T_P^* in Eq. 3' matches with that in A.3 (or the left and right terms of A.4 match together). This process is intensive when being applied to a wide range of v^* .

In our study, an approximation of z_0^* with respect to v^* was obtained to expedite the process, expressed by Eq. A.5. This approximation has a maximum error of 10% as compared to the manual incrementation method.

$$t_p^* = 0.2069 \times c^{(-1.486)}$$
 (A.5)

where

$$c = \frac{v^* \cdot \tan^{-1}(\sqrt{\frac{8}{v^*}})}{2\sqrt{\pi}}$$
 (A.6)

 z_0 *can be then calculated based on A.2, as:

$$z_o^* = \sqrt{\frac{2.t_p^{*2} + t_p^*}{2.t_p^* + 2.}} \tag{A.7}$$

It should be noted that the procedure to figure out z_0^* is considered at $z^*=0$. To further construct the melting and vaporising boundaries, the corresponding melting depth equal to one layer thickness l should be considered, which is $z^*=l/r_B$. Therefore, for a given v^* , a z_0^* will be firstly estimated. Then, the normalised time t^* required to reach the peak temperature at the depth z^* can be calculated by Eq. A.2 by substituting the respective z_0^* and z^* . Finally, the normalised net power q^*_{net} required to achieve melting ($T^*_m=1$) or vaporising ($T^*_v=2$) of a given v^* is calculated via equation Eq. 4' by substituting all relevant variables t^* , z^* , z_0^* and $T^*_{m/v}$.

$$q_{net}^* = \left(-2z^*L_{m/v}^* + \frac{T_{m/v}^* \times [t^*(t^*+1)]^{\frac{1}{2}}}{\binom{2}{\pi}} \times \exp\left[\frac{\left(z^* + z_0^*\right)^2}{t^*}\right]\right) \times v^*$$

$$(4')$$

By applying Eq. 4' on a range of v^* (e.g., 1–100), the respective melting and vaporising boundaries can be constructed to create the normalised process diagram. It is worth noting that changing layer thickness l or beam radius r_B results in the shifting of the calculated boundaries. Parameter sets represented by the dimensionless beam power q^* and dimensionless beam velocity v^* can be plotted against the diagram to evaluate their effect on part density or cracking density. In a reverse way, good processing parameters can be selected on the diagram and converted back to the respective laser power P and scan speed v.

Appendix B. Characterisation of hot cracking for samples of DOE 1 to DOE 3 for the case study on CM247LC

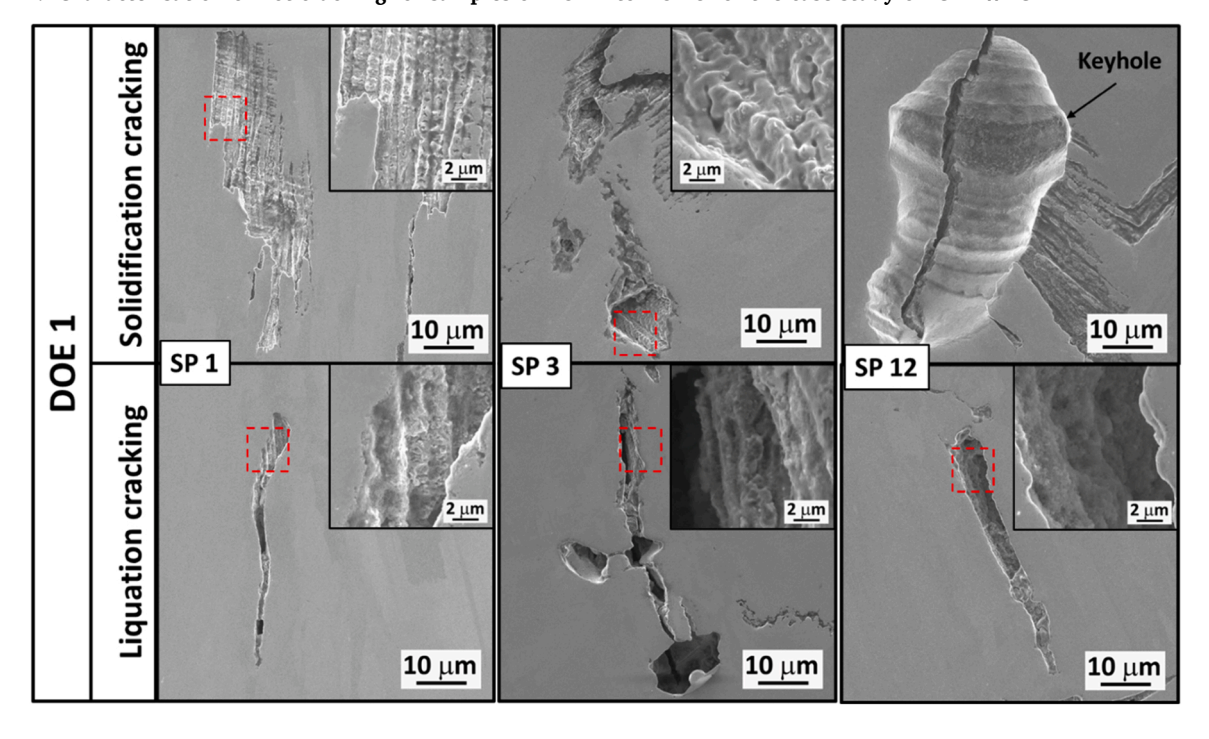


Fig. B1. Solidification cracking and liquation cracking were characterised for selected samples of DOE 1. Interaction between a keyhole pore and solidification cracks can be observed in SP 12.

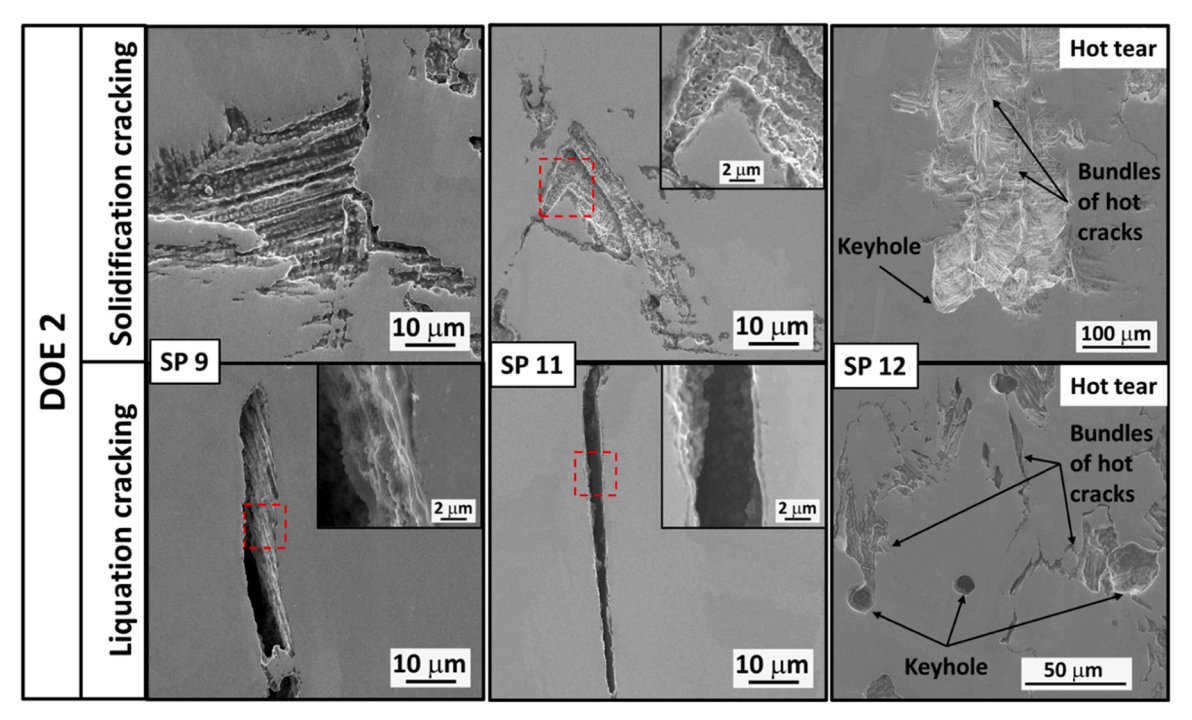


Fig. B2. Solidification cracking and liquation cracking were characterised for selected samples of DOE 2. Hot tears were depicted for SP 12 showing interaction between keyhole pores and solidification cracks. Note that the scale bars of SP 12 images are different from others.

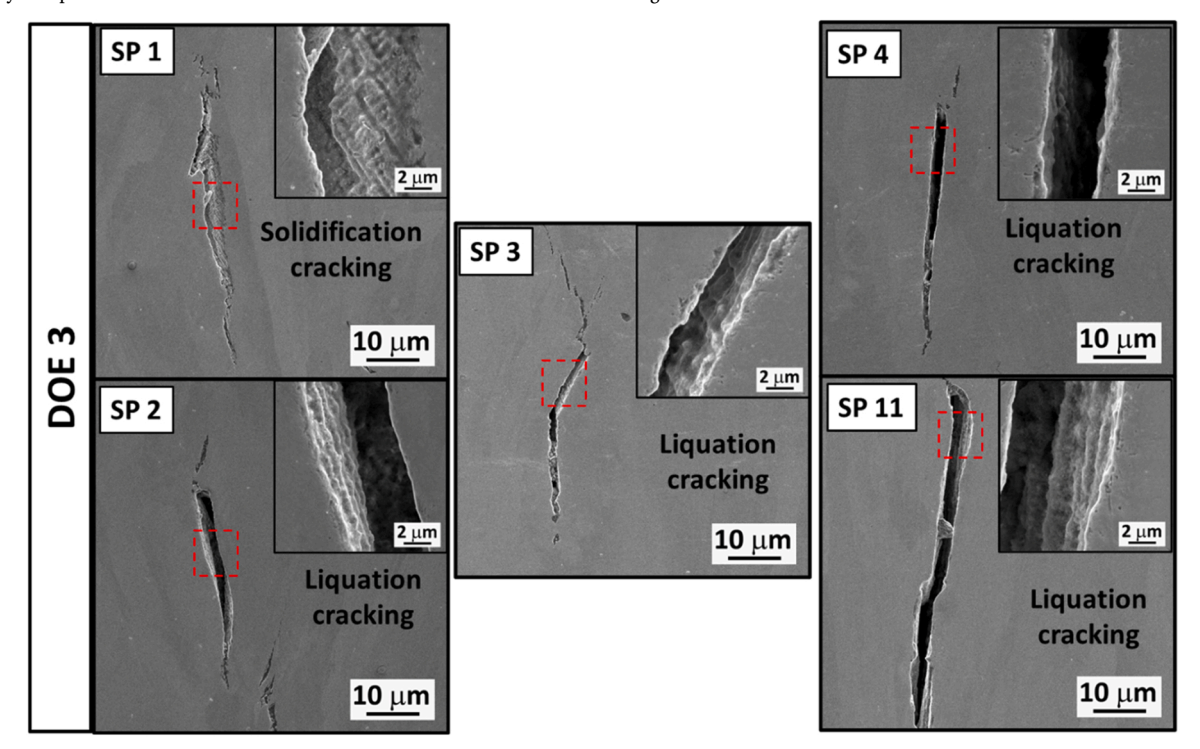


Fig. B3. Solidification cracking and liquation cracking were characterised for selected samples of DOE 3. It is challenging to identify solidification cracking in DOE 3, which may be due to the reducing de/dT values.

References

- A. Huxol, F.-J. Villmer, Experimental approach towards parameter evaluation in laser powder bed fusion of metals, Int. J. Comput. Integr. Manuf. vol. 35 (4-5) (2021) 556–567.
- [2] I.F. Ituarte, E. Coatanea, M. Salmi, J. Tuomi, J. Partanen, Additive manufacturing in production: a study case applying technical requirements, Phys. Procedia vol. 78 (2015) 357–366.
- [3] Z. Li, I. Kucukkoc, D.Z. Zhang, F. Liu, Optimising the process parameters of selective laser melting for the fabrication of Ti6Al4V alloy, Rapid Prototyp. J. (2018).
- [4] C.L. Druzgalski, A. Ashby, G. Guss, W.E. King, T.T. Roehling, M.J. Matthews, Process optimization of complex geometries using feed forward control for laser powder bed fusion additive manufacturing, Addit. Manuf. vol. 34 (2020).
- [5] H. Yeung, B. Lane, J. Fox, Part geometry and conduction-based laser power control for powder bed fusion additive manufacturing, Addit. Manuf. vol. 30 (Dec 2019).
- [6] M. Ashby, K.E. Easterling, The transformation hardening of steel surfaces by laser beams—I. Hypo-eutectoid steels, Acta Metall. vol. 32 (11) (1984) 1935–1948.

- [7] J.C. Ion, K.E. Easterling, M. Ashby, A second report on diagrams of microstructure and hardness for heat-affected zones in welds, Acta Metall. vol. 32 (11) (1984) 1949–1962.
- [8] J.C. Ion, H.R. Shercliff, M.F. Ashby, Diagrams for laser materials processing, Acta Metall. Et. Mater. vol. 40 (7) (1992) 1539–1551.
- [9] D.B. Hann, J. Iammi, J. Folkes, A simple methodology for predicting laser-weld properties from material and laser parameters, J. Phys. D: Appl. Phys. vol. 44 (44) (2011)
- [10] W.E. King, et al., Observation of keyhole-mode laser melting in laser powder-bed fusion additive manufacturing, J. Mater. Process. Technol. vol. 214 (12) (2014) 2915–2925.
- [11] A.M. Rubenchik, W.E. King, S.S. Wu, Scaling laws for the additive manufacturing, J. Mater. Process. Technol. vol. 257 (2018) 234–243.
- [12] Y. Yang, et al., Validated dimensionless scaling law for melt pool width in laser powder bed fusion, J. Mater. Process. Technol. vol. 299 (2022).
- [13] M. van Elsen, F. Al-Bender, J.P. Kruth, Application of dimensional analysis to selective laser melting, Rapid Prototyp. J. vol. 14 (1) (2008) 15–22.
- [14] T. Mukherjee, V. Manvatkar, A. De, T. DebRoy, Dimensionless numbers in additive manufacturing, J. Appl. Phys. vol. 121 (6) (2017).
- [15] M. Thomas, G.J. Baxter, I. Todd, Normalised model-based processing diagrams for additive layer manufacture of engineering alloys, Acta Mater. vol. 108 (2016) 26-35.
- [16] T. Mukherjee, J.S. Zuback, A. De, T. DebRoy, Printability of alloys for additive manufacturing, Sci. Rep. vol. 6 (Jan 22 2016) 19717.
- [17] J. Ye, et al., Energy coupling mechanisms and scaling behavior associated with laser powder bed fusion additive manufacturing, Adv. Eng. Mater. vol. 21 (7) (2019) 1900185.
- [18] M. Bayat, et al., Keyhole-induced porosities in Laser-based Powder Bed Fusion (L-PBF) of Ti6Al4V: High-fidelity modelling and experimental validation, Addit. Manuf. vol. 30 (2019).
- [19] S.D. Jadhav, L.R. Goossens, Y. Kinds, B.V. Hooreweder, K. Vanmeensel, Laser-based powder bed fusion additive manufacturing of pure copper, Addit. Manuf. vol. 42 (2021) 101990. /06/01/ 2021.
- [20] S. Guo, W. Zhou, Z. Zhou, N. Nomura, Laser additive manufacturing of pure molybdenum using freeze-dry pulsated orifice ejection method-produced powders, J. Mater. Res. Technol. vol. 16 (2022) 1508–1516.
- [21] H.R. Shercliff, M. Ashby, The prediction of case depth in laser transformation hardening, Metall. Trans. A vol. 22 (1991) 2459–2466.
- [22] E.A. Brandes, G. Brook, Chapter 14 General Physical Properties. Smithells metals reference book, Elsevier, 2013, pp. 1040–1082.
- [23] D. Rosenthal, Mathematical theory of heat distribution during welding and cutting, Weld. J. vol. 20 (5) (1941) 220s–234s.
- [24] D. Rosenthal, The theory of moving sources of heat and its application to metal treatments, Trans. Am. Soc. Mech. Eng. vol. 68 (8) (1946) 849–865.
- [25] N. Prokhorov, The problem of the strength of metals while solidifying during welding, Svarochnoe Proizv. vol. 6 (1956) 5–11.
- [26] T. Kannengiesser, T. Boellinghaus, Hot cracking tests—an overview of present technologies and applications, Weld. World vol. 58 (3) (2014) 397–421. /05/01 2014
- [27] N. Coniglio, C.E. Cross, Initiation and growth mechanisms for weld solidification cracking, Int. Mater. Rev. vol. 58 (7) (2013) 375–397.
- [28] Y. Chen, et al., Microstructure characterization and mechanical properties of crack-free Al-Cu-Mg-Y alloy fabricated by laser powder bed fusion, Addit. Manuf. vol. 58 (2022).
- [29] T. Raza, J. Andersson, L.-E. Svensson, Varestraint Testing of Selective Laser Additive Manufactured Alloy 718—Influence of Grain Orientation, Metals vol. 9 (10) (2019).
- [30] S. Lee, J. Kim, J. Choe, S.-W. Kim, J.-K. Hong, Y.S. Choi, Understanding Crack Formation Mechanisms of Ti–48Al–2Cr–2Nb Single Tracks During Laser Powder Bed Fusion, Met. Mater. Int. vol. 27 (1) (2020) 78–91.
- [31] T. Huynh, Parametric Investigation and Optimization for Inconel 718 Nickel-Based Superalloy in Laser Powder Bed Fusion, 2020.
- [32] N. Saunders, U. Guo, X. Li, A. Miodownik, J.-P. Schillé, Using JMatPro to model materials properties and behavior, Jom vol. 55 (2003) 60–65.
- [33] K. Georgilas, R.H.U. Khan, M.E. Kartal, The influence of pulsed laser powder bed fusion process parameters on Inconel 718 material properties, Mater. Sci. Eng.: A vol. 769 (2020).
- [34] Aubert&Duval. (2020, 10/10/2023). Stellar ABD-900AM Datasheet. Available: (https://www.aubertduval.com/wp-media/uploads/sites/2/2019/09/ABD-900 AM_Stellar_AM_V0_GB.pdf).
- [35] O. Adegoke, J. Andersson, H. Brodin, R. Pederson, Influence of Laser Powder Bed Fusion Process Parameters on Voids, Cracks, and Microhardness of Nickel-Based Superalloy Alloy 247LC, Mater. (Basel) vol. 13 (17) (2020).
- [36] L. Avala, M. Bheema, P.K. Singh, R. Ray, S. Srivastaba, Measurement of thermophysical properties of Ni based super alloys, ISSN (Print.) (2321-5747) vol. 1 (2013) 108e112.
- [37] N. Diaz Vallejo, C. Lucas, N. Ayers, K. Graydon, H. Hyer, Y. Sohn, Process Optimization and Microstructure Analysis to Understand Laser Powder Bed Fusion of 316L Stainless Steel, Metals vol. 11 (5) (2021).
- [38] J.P.M. Pragana, et al., Influence of processing parameters on the density of 316L stainless steel parts manufactured through laser powder bed fusion, Proc. Inst. Mech. Eng., Part B: J. Eng. Manuf. vol. 234 (9) (2020) 1246–1257.
- [39] A. Leicht, M. Rashidi, U. Klement, E. Hryha, Effect of process parameters on the microstructure, tensile strength and productivity of 316L parts produced by laser powder bed fusion, Mater. Charact. vol. 159 (2020).

- [40] E. Yasa, İ. Atik, İ. Kandemir, Material-specific phenomena and developing higher yield process parameters in laser powder bed fusion of 17-4 PH stainless steel, J. Braz. Soc. Mech. Sci. Eng. vol. 45 (1) (2023) 38.
- [41] Matweb. (31/07/2023). 17-4PH Thermophysical properties. Available: (https://www.matweb.com/search/datasheet.aspx?matguid=ef0844b850954281a438dc76c1e0b49e&ckck=1).
- [42] J. Bae, M.-k Kim, E. Oh, K.-T. Yang, J. Suhr, Experimental and numerical investigation of 17–4PH stainless steel fabricated by laser powder bed fusion and hot isostatic pressing, Mater. Res. Express vol. 8 (10) (2021) 106512.
- [43] Z. Hu, H. Zhu, H. Zhang, X. Zeng, Experimental investigation on selective laser melting of 17-4PH stainless steel, Opt. Laser Technol. vol. 87 (2017) 17–25.
- [44] P. Promoppatum, et al., Quantification and prediction of lack-of-fusion porosity in the high porosity regime during laser powder bed fusion of Ti-6Al-4V, J. Mater. Process, Technol. vol. 300 (2022) 117426.
- [45] J. Dilip, et al., Influence of processing parameters on the evolution of melt pool, porosity, and microstructures in Ti-6Al-4V alloy parts fabricated by selective laser melting, Prog. Addit. Manuf. vol. 2 (2017) 157–167.
- [46] W.H. Kan, et al., The influence of porosity on Ti-6Al-4V parts fabricated by laser powder bed fusion in the pursuit of process efficiency, Int. J. Adv. Manuf. Technol. vol. 119 (7-8) (2022) 5417–5438.
- [47] H. Gong, K. Rafi, T. Starr, and B. Stucker, The Effects of Processing Parameters on Defect Regularity in Ti-6Al-4V Parts Fabricated By Selective Laser Melting and Electron Beam Melting, in 24th Annual International Solid Freeform Fabrication Symposium—An Additive Manufacturing Conference, Austin, TX, Aug, 2013, pp. 12-14
- [48] M. Colopi, A.G. Demir, L. Caprio, B. Previtali, Limits and solutions in processing pure Cu via selective laser melting using a high-power single-mode fiber laser, Int. J. Adv. Manuf. Technol. vol. 104 (5) (2019) 2473–2486. /10/01 2019.
- [49] Matweb. (2023). Copper thermophysical properties. Available: (https://www.matweb.com/search/datasheet_print.aspx?matguid=9aebe83845c04c1db5126fada 6f76f7e).
- [50] M. Abdelhafiz, K.S. Al-Rubaie, A. Emadi, M.A. Elbestawi, Process-Structure-Property Relationships of Copper Parts Manufactured by Laser Powder Bed Fusion, Materials vol. 14 (11) (2021) 2945.
- [51] M. Bonesso, et al., Effect of Particle Size Distribution on Laser Powder Bed Fusion Manufacturability of Copper, BHM Berg. - und H. üttenmännische Mon. vol. 166 (5) (2021) 256–262. /05/01 2021.
- [52] P. Rebesan, et al., Pure molybdenum manufactured by Laser Powder Bed Fusion: Thermal and mechanical characterization at room and high temperature, Addit. Manuf. vol. 47 (2021) 102277. /11/01/ 2021.
- [53] Plansee. Mo Thermo-physical properties. Available: (https://www.plansee.com/en/materials/molybdenum.html).
- [54] M. Higashi, T. Ozaki, Selective laser melting of pure molybdenum: Evolution of defect and crystallographic texture with process parameters, Mater. Des. vol. 191 (2020) 108588. /06/01/2020.
- [55] B.T. Gibson, R.A. Lowden, Process Development for Selective Laser Melting of Molybdenum, Oak Ridge National Lab.(ORNL), Oak Ridge, TN (United States), 2018.
- [56] P. Bajaj, Disertation, The University of Sheffield, SLM Manuf. molybdenum (2016).
- [57] M. Sokolova, G. Lapalme, A systematic analysis of performance measures for classification tasks, Inf. Process. Manag. vol. 45 (4) (2009) 427–437.
- [58] I.M. De Diego, A.R. Redondo, R.R. Fernández, J. Navarro, J.M. Moguerza, General Performance Score for classification problems, Appl. Intell. vol. 52 (10) (2022) 12049–12063.
- [59] A. Luque, A. Carrasco, A. Martín, A. de las Heras, The impact of class imbalance in classification performance metrics based on the binary confusion matrix, Pattern Recognit. vol. 91 (2019) 216–231.
- [60] E.-J. Chun, Y.-S. Jeong, K.-M. Kim, H. Lee, S.-M. Seo, Suppression of liquation cracking susceptibility via pre-weld heat treatment for manufacturing of CM247LC superalloy turbine blade welds, J. Adv. Join. Process. vol. 4 (2021).
- [61] M. Khorasani, et al., The effect of absorption ratio on meltpool features in laser-based powder bed fusion of IN718, Opt. Laser Technol. vol. 153 (2022).
- [62] J. Liu, P. Wen, Metal vaporization and its influence during laser powder bed fusion process, Mater. Des. vol. 215 (2022).
- [63] H. Zheng, H. Li, L. Lang, S. Gong, Y. Ge, Effects of scan speed on vapor plume behavior and spatter generation in laser powder bed fusion additive manufacturing, J. Manuf. Process. vol. 36 (2018) 60–67.
- [64] I. Bitharas, N. Parab, C. Zhao, T. Sun, A.D. Rollett, A.J. Moore, The interplay between vapour, liquid, and solid phases in laser powder bed fusion, Nat. Commun. vol. 13 (1) (2022) 2959.
- [65] P.Y. Shcheglov, A. Gumenyuk, I.B. Gornushkin, M. Rethmeier, V. Petrovskiy, Vapor–plasma plume investigation during high-power fiber laser welding, Laser Phys. vol. 23 (1) (2012) 016001.
- [66] Y. Kawahito, K. Kinoshita, N. Matsumoto, S. Katayama, Visualization of refraction and attenuation of near-infrared laser beam due to laser-induced plume, J. Laser Appl. vol. 21 (2) (2009) 96–101.
- [67] N. Kouraytem, et al., Solidification crack propagation and morphology dependence on processing parameters in AA6061 from ultra-high-speed x-ray visualization, Addit. Manuf. vol. 42 (2021).
- [68] D.T. Rees, et al., In situ X-ray imaging of hot cracking and porosity during LPBF of Al-2139 with TiB2 additions and varied process parameters, Mater. Des. (2023) 112031.
- [69] L.N. Carter, Selective laser melting of nickel superalloys for high temperature applications, University of Birmingham, 2013.

- [70] D. Abe, F. Matsuzaka, Y. Murakami, T. Matsuoka, H. Yamaoka, Determining the BTR by conducting a Trans-Varestraint test using a high-speed camera and twocolor pyrometry, Weld. World vol. 62 (6) (2018) 1237–1246.
- [71] D. Statharas, H. Atkinson, R. Thornton, J. Marsden, H. Dong, S. Wen, Getting the Strain Under Control: Trans-Varestraint Tests for Hot Cracking Susceptibility, Metall. Mater. Trans. A vol. 50 (4) (2019) 1748–1762.
- [72] A. Kromm, M. Thomas, T. Kannengiesser, J. Gibmeier, F. Vollert, Assessment of the Solidification Cracking Susceptibility of Welding Consumables in the Varestraint Test by Means of an Extended Evaluation Methodology, Adv. Eng. Mater. vol. 24 (6) (2022).
- [73] J.C. Lippold, Welding Metallurgy and Weldability, Wiley Online Library, 2015.